AIM/CD5L attenuates DAMPs in the injured brain and thereby ameliorates ischemic stroke

Natsumi Maehara, Kaori Taniguchi, Ami Okuno, Hideaki Ando, Aika Hirota, Zhizeng Li, Ching-Ting Wang, Satoko Arai, Toru Miyazaki

Cell Reports

Article

AIM/CD5L attenuates DAMPs in the injured brain and thereby ameliorates ischemic stroke

Graphical abstract

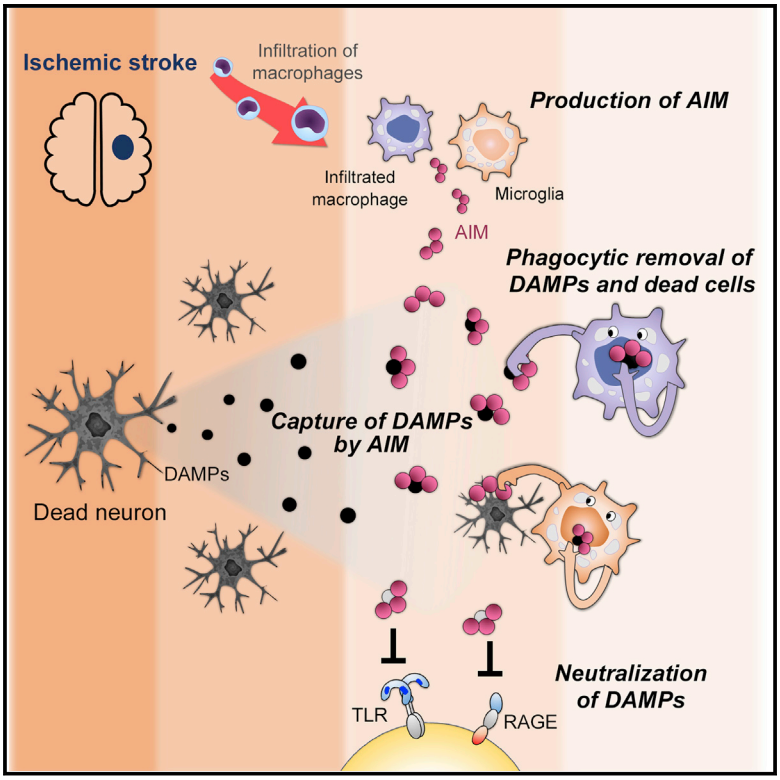

Highlights

- AIM markedly increases in the infarcted brain, expressed by recruited macrophages
- AIM associates with DAMPs via charge-based interaction and disulfide bond formation
- AIM reduces or attenuates DAMPs, thereby suppressing cerebral inflammation
- Administration of AIM improves the post-stroke prognosis in mice

Authors

Natsumi Maehara, Kaori Taniguchi, Ami Okuno, ..., Ching-Ting Wang, Satoko Arai, Toru Miyazaki

Correspondence

sarai@m.u-tokyo.ac.jp (S.A.), tm@m.u-tokyo.ac.jp (T.M.)

In brief

Maehara et al. show that AIM (or CD5L) is increased in the infarcted brain and associates with DAMPs. The association decreases DAMPs, and therefore, AIM improves post-stroke prognosis in mice by reducing cerebral inflammation. AIM may be a useful therapy for ischemic stroke targeting DAMP-mediated sterile inflammation.

Maehara et al., 2021, Cell Reports *36*, 109693
September 14, 2021
https://doi.org/10.1016/j.celrep.2021.109693

CellPress

Cell Reports

CellPress
OPEN ACCESS

Article

AIM/CD5L attenuates DAMPs in the injured brain and thereby ameliorates ischemic stroke

Natsumi Maehara,[1] Kaori Taniguchi,[1,4] Ami Okuno,[1,4] Hideaki Ando,[1,4] Aika Hirota,[1] Zhiheng Li,[1] Ching-Ting Wang,[1] Satoko Arai,[1,*] and Toru Miyazaki[1,2,3,5,*]

[1]Laboratory of Molecular Biomedicine for Pathogenesis, Center for Disease Biology and Integrative Medicine, Faculty of Medicine, The University of Tokyo, Tokyo 113-0033, Japan

[2]LEAP, Japan Agency for Medical Research and Development, Tokyo 113-0033, Japan

[3]Laboratoire d'ImmunoRhumatologie Moléculaire, Plateforme GENOMAX, Institut National de la Santé et de la Recherche Médicale UMR_S 1109, Faculté de Médecine, Fédération Hospitalo-Universitaire OMICARE, Fédération de Médecine Translationnelle de Strasbourg, Laboratory of Excellence TRANSPLANTEX, Université de Strasbourg, Strasbourg, France

[4]These authors contributed equally

[5]Lead contact

*Correspondence: sarai@m.u-tokyo.ac.jp (S.A.), tm@m.u-tokyo.ac.jp (T.M.)

https://doi.org/10.1016/j.celrep.2021.109693

SUMMARY

The sterile inflammation caused by damage-associated molecular patterns (DAMPs) worsens the prognosis following primary injury such as ischemic stroke. However, there are no effective treatments to regulate DAMPs. Here, we report that AIM (or CD5L) protein reduces sterile inflammation by attenuating DAMPs and that AIM administration ameliorates the deleterious effects of ischemic stroke. AIM binds to DAMPs via charge-based interactions and disulfide bond formation. This AIM association promotes the phagocytic removal of DAMPs and neutralizes DAMPs by impeding their binding to inflammatory receptors. In experimental stroke, AIM-deficient mice exhibit severe neurological damage and higher mortality with greater levels of DAMPs and associated inflammation in the brain than wild-type mice, in which brain AIM levels increase following stroke onset. Recombinant AIM administration reduces sterile inflammation in the infarcted region, leading to a profound reduction of animal mortality. Our findings provide a basis for the therapies targeting DAMPs to improve ischemic stroke.

INTRODUCTION

The inefficient removal of dead cells and their debris results in the release of intracellular inflammatory agents, so-called damage-associated molecular patterns (DAMPs) (Kono and Rock, 2008; Chen and Nuñez, 2010; Zindel and Kubes, 2020). Although DAMPs are normal endogenous intracellular proteins, and therefore hidden from recognition by the immune system, once released into the extracellular environment, they bind to pattern recognition receptors, including Toll-like receptors (TLRs) and receptor for advanced glycation end-products (RAGE), and activate innate immunity to induce the production of inflammatory cytokines in the absence of microorganisms (Medzhitov, 2008; Kumar et al., 2013; Gülke et al., 2018; Hudson and Lippman, 2018). This process is called sterile inflammation, which is often caused by ischemia-reperfusion injury (IRI), trauma, or chemically induced injury (Kono and Rock, 2008; Chen and Nuñez, 2010; Zindel and Kubes, 2020).

Ischemic stroke, one of the most common causes of severe disability and death globally (Lane and Bailey, 2005; Dayon et al., 2011), and currently featured as an important complication of coronavirus disease 2019 (COVID-19) (Trejo-Gabriel-Galán, 2020; Oxley et al., 2020; Tan et al., 2020), is typically associated with sterile inflammation (Lane and Bailey, 2005; Dayon et al., 2011; Gülke et al., 2018). There is a widely accepted consensus that the prognosis of ischemic stroke is highly influenced by the state of sterile inflammation in the affected brain after the onset of stroke. Because currently available therapies, such as thrombolysis and thrombectomy, do not always profoundly improve the prognosis of stroke patients, increasing attention has recently been paid to post-stroke sterile inflammation as a therapeutic target (Iadecola and Anrather, 2011; Chamorro et al., 2016; Gülke et al., 2018; Land, 2020). Of the different types of DAMPs, recent evidence shows that peroxiredoxin (PRDX; particularly PRDX1) (Riddell et al., 2010; Robinson et al., 2010; Shichita et al., 2012; Richard et al., 2016), high-mobility-group-box 1 (HMGB1) (Qiu et al., 2008; Hayakawa et al., 2010), and S100 calcium-binding proteins (S100) (Passey et al., 1999; Engel et al., 2000; Ziegler et al., 2009; Saksi et al., 2011) are highly involved in post-stroke sterile inflammation in the brain. More recently, it has been reported that as a repair process, DAMPs are physiologically internalized by microglia/macrophages and infiltrating myeloid cells through macrophage scavenger receptor 1, whose expression is regulated by MAF bZIP transcription factor B (MafB) (Shichita et al., 2017). However, no effective stroke treatments based on DAMP removal have been established.

Apoptosis inhibitor of macrophage (AIM; also called CD5 antigen-like [CD5L]) is a circulating protein produced by tissue macrophages, which we initially identified as a supporter of macrophage survival (Miyazaki et al., 1999). AIM is now recognized as a facilitator of repair processes in many diseases (Kurokawa et al., 2010; Maehara et al., 2014; Wang et al., 2015; Arai et al., 2016; Tomita et al., 2017; Arai and Miyazaki, 2018), in particular, IRI-induced acute kidney injury (AKI) (Arai et al., 2016), whose central pathology is physical obstruction of renal tubules by dead epithelial cells and the associated sterile inflammation induced by dead cell-derived DAMPs (Humphreys et al., 2008; Bonventre and Yang, 2011; Kusaba et al., 2014). Of the various mechanisms of action of AIM, the enhanced phagocytic removal of dead cells is highlighted during the repair of AKI. AIM consists of three cysteine-rich domains (termed the SRCR domains) (Miyazaki et al., 1999), and a unique positively charged amino acid cluster is present at the carboxyl terminus within the third SRCR domain (Miyazaki et al., 1999; Hiramoto et al., 2018). This cluster develops charge-based interactions with dead cells, whose surface is strongly negatively charged because of the high levels of exposed phosphatidylserine (Arai et al., 2016; Tomita et al., 2017). This association highly enhances the engulfment of dead cells by phagocytes, as AIM is highly internalized by phagocytes via multiple scavenger receptors (Arai and Miyazaki, 2018). Indeed, intravenous injection of recombinant AIM (rAIM) protein markedly improves IRI-induced AKI in mice by promoting the phagocytic removal of intratubular dead cell debris (Arai et al., 2016). Pathologic similarities between ischemic stroke and IRI-induced AKI, namely, initial cell death and subsequent sterile inflammation caused by DAMPs, as well as the involvement of phagocytes in the recovery process, led us to assess the possible impact of AIM on the pathophysiology of ischemic stroke.

RESULTS AND DISCUSSION

The increase in brain AIM following onset of ischemic stroke

Although *AIM* (*cd5l*) mRNA expression was not detected in the brain of healthy mice, its significant increase was observed by quantitative PCR (qPCR) after mice underwent transient middle cerebral artery occlusion (MCAO) to induce stroke laterally (Figure 1A). *AIM* mRNA was specifically expressed by $CD11b^+$ microglia/macrophages, as evidenced in further assessments using $CD11b^+$ and $CD11b^-$ cells isolated from infarcted brain (Figure 1A). Consistently, up to 250 ng/mg tissue of AIM protein was present in the affected brain on day 7 after MCAO when assessed using enzyme-linked immunosorbent assay (ELISA) using brain tissue lysates, though no increase of AIM protein was observed in the unaffected brain (Figure 1B). Mice deficient in MafB specifically in macrophages (Lysm-Cre;$MafB^{-/-}$) (Shawki et al., 2018) have been shown to develop severe brain damage after MCAO (Shichita et al., 2017). The increase in *AIM* mRNA levels triggered by MCAO was partly abrogated in Lysm-Cre;$MafB^{-/-}$ mice, in line with the fact that MafB is one of the major transcription factors regulating *AIM* expression (Hamada et al., 2014) (Figure 1C).

In line with the increase of AIM expression, the microtubule-associated protein 2 (MAP2)-negative dead neural cell area was strongly stained for AIM on day 7 after MCAO when assessed using immunohistochemistry (IHC) (Figure 1D). This situation is reminiscent of the accumulation of AIM on intratubular dead epithelial cell debris observed during AKI, along with the ability of AIM to bind well to dead cell debris (Arai et al., 2016). Similar AIM accumulation in the infarcted area was also observed in the brain of human stroke patients (Figure 1E). Under higher magnification, high levels of AIM were observed in Iba1-positive macrophage-like cells (indicated by arrows) in mouse and human brains (Figures 1D and 1E), confirming the qPCR results that showed increased *AIM* mRNA expression in $CD11b^+$ cells presented in Figure 1A. Iba1-positive macrophages infiltrating the infarcted area (negative for MAP2) were stained with oil red O, indicating that they were actively engulfing dead cell debris (David and Kroner, 2011; Kawabori et al., 2015) (Figure 2). In contrast, in AIM-deficient ($AIM^{-/-}$) mice challenged with MCAO, although the volume of the infarcted area and the number of infiltrating macrophages were comparable with those in wild-type mice (Figure S1), macrophages in the infarcted region were largely negative for oil red O, suggesting that as in AKI, AIM contributes to the phagocytic removal of dead cell debris in the infarcted region (Figure 2).

AIM reduced DAMPs at the infarcted area and reduced the associated brain inflammation

In addition, IHC analysis of the brain post-MCAO revealed significantly larger number of positive signals for extracellular PRDX1 (which were not co-localized with cell bodies and nuclei) in the infarcted area in $AIM^{-/-}$ mice compared with wild-type mice (Figure 3A, brown dots in IHC). More impressively, daily intravenous injection of rAIM (0.5 mg/mouse) immediately after MCAO reduced PRDX1 in both wild-type and $AIM^{-/-}$ mice (Figure 3A), though the number of infiltrating macrophages was not influenced by rAIM injection (Figure S1). The blood-brain barrier (BBB) is known to be temporally and partly disrupted during the acute phase of ischemic stroke (Zou et al., 2015; Choi et al., 2016). Indeed, brain tissue from $AIM^{-/-}$ mice stained widely for AIM after rAIM injection at day 3 post-MCAO, indicating that the injected rAIM passed through the BBB (Figure S2). Such correlation in the decrease of PRDX1 and the presence of brain AIM was more obvious on day 3 than day 7 (Figure 3A, graphs). Levels of HMGB1 and S100A9, which are also major pathogenic DAMPs related to stroke, were decreased in the infarcted region at day 7 than at day 3 in wild-type mice, along with the increase of brain AIM levels post-MCAO, though its reduction in wild-type mice compared with $AIM^{-/-}$ mice, or following rAIM injection, was not as pronounced as for the PRDX1 examined (Figure S3). It is noteworthy, however, that many $AIM^{-/-}$ mice had a rapid decline of health and died before day 3 after MCAO, and that their infarcted regions in the brain before their death (on day 2 to day 3) contained a markedly larger number of strong signals for S100A9 than the healthier $AIM^{-/-}$ mice (Figure 3B). Note that no wild-type mice died before day 3 (a comparison of mortality in wild-type and $AIM^{-/-}$ mice is presented later).

CellPress
OPEN ACCESS

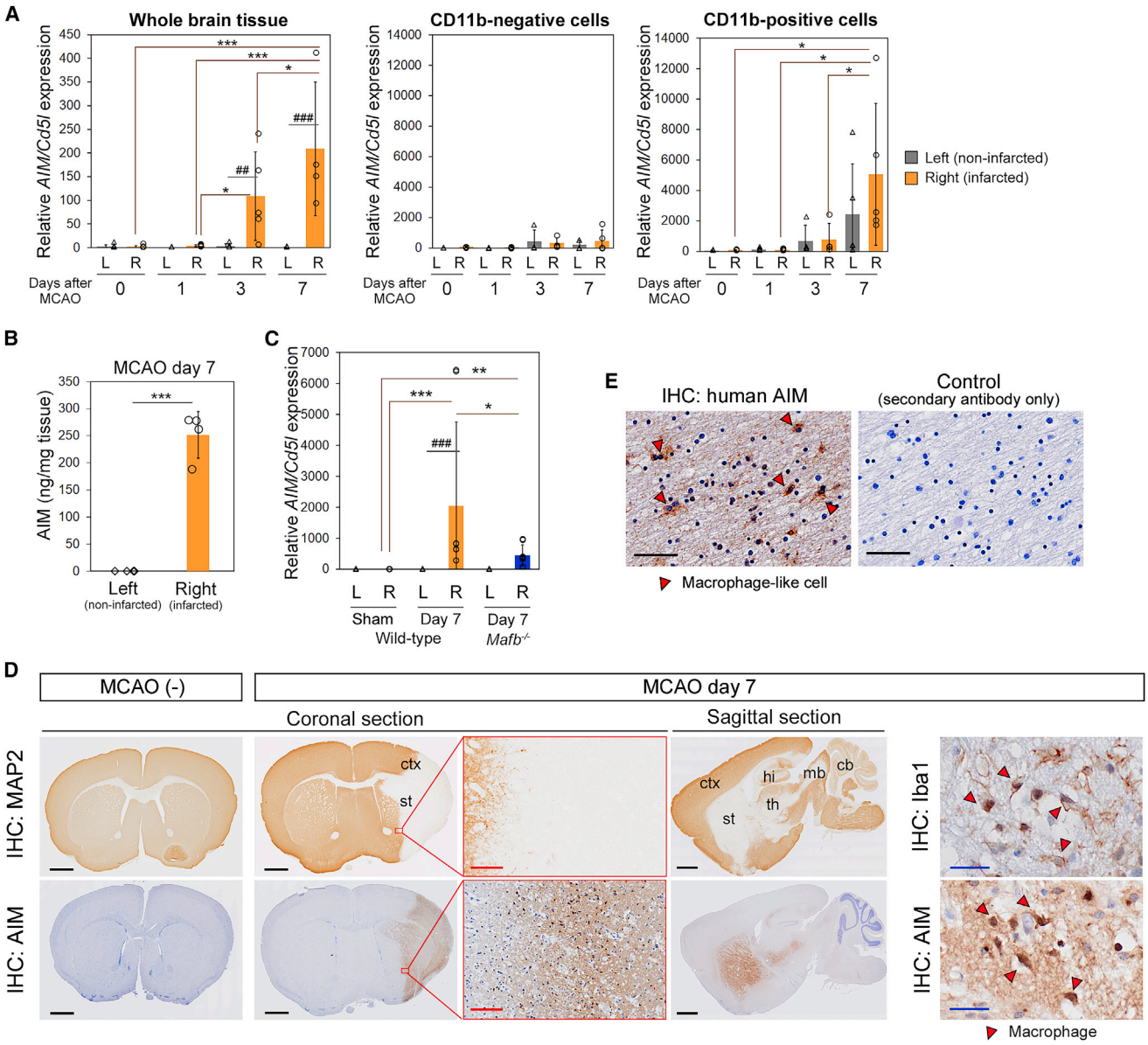

Figure 1. AIM expression in the infarcted brain

(A) qPCR analysis of *AIM* (*Cd5l*) mRNA levels in the brain using RNA isolated from whole tissue or dissociated cells by CD11b (macrophage/myeloid marker) expression from wild-type mice on days 1, 3, and 7 after MCAO. L, left lobe, non-infarcted; R, right lobe, infarcted. Relative values to that of whole tissue before MCAO (Pre) are shown. Bars denote SD of the mean. Statistics: multi-way ANOVA followed by Bonferroni's post hoc test. *$p < 0.05$, **$p < 0.01$, and ***$p < 0.001$ (between the values at different days in the left or right lobe); $^{\#\#}p < 0.01$ and $^{\#\#\#}p < 0.001$ (between the values in the left and right lobes at the same day). n = 4 or 5.

(B) The amount of AIM protein in the brain was analyzed using ELISA using lysates from the infarcted (right lobe [R]) and non-infarcted (left lobe [L]) brain. Values are presented as μg AIM/mg brain. n = 4.

(C) qPCR analysis of *AIM* (*Cd5l*) mRNA levels in the brain using RNA isolated from whole tissue from wild-type mice and Lysm-Cre;*MafB*$^{-/-}$ (*MafB*$^{-/-}$) mice on day 7 after MCAO. Relative values to the average of those for sham samples are shown. L, left lobe, non-infarcted; R, right lobe, infarcted. Bars denote SD of the mean. Statistics: multi-way ANOVA followed by Bonferroni's post hoc test. *$p < 0.05$, **$p < 0.01$, and ***$p < 0.001$ (values in sham versus those on day 7 in each mouse type); $^{\#\#\#}p < 0.001$ (values in the left versus right in each group). n = 8–10.

(D) IHC analysis of AIM in brain specimens from day 7 post-MCAO wild-type mice. The infarcted area, which is negative for MAP2, was stained for AIM. A part of striatum (red square) is shown at a higher magnification for AIM and MAP2 (third lane, squared by red line). The right panels depict the serial section stained for Iba1 and AIM presented at high magnification. Iba1-positive macrophages are strongly positive for AIM. ctx, cortex; st, striatum; hi, hypothalamus; th, thalamus; mb, mid brain; cb, cerebrum. Black bars, 1 mm; red bars, 100 μm; blue bars, 5 μm.

(E) A human brain specimen from an infarcted region was stained for AIM. A control staining with only secondary antibody is also presented (lower panel). Note that whole area was MAP2 negative (data not presented). The strong staining for AIM indicates AIM production in macrophages (determined by their shape; indicated by arrows), in accordance with the qPCR data shown in (A). Bars, 50 μm.

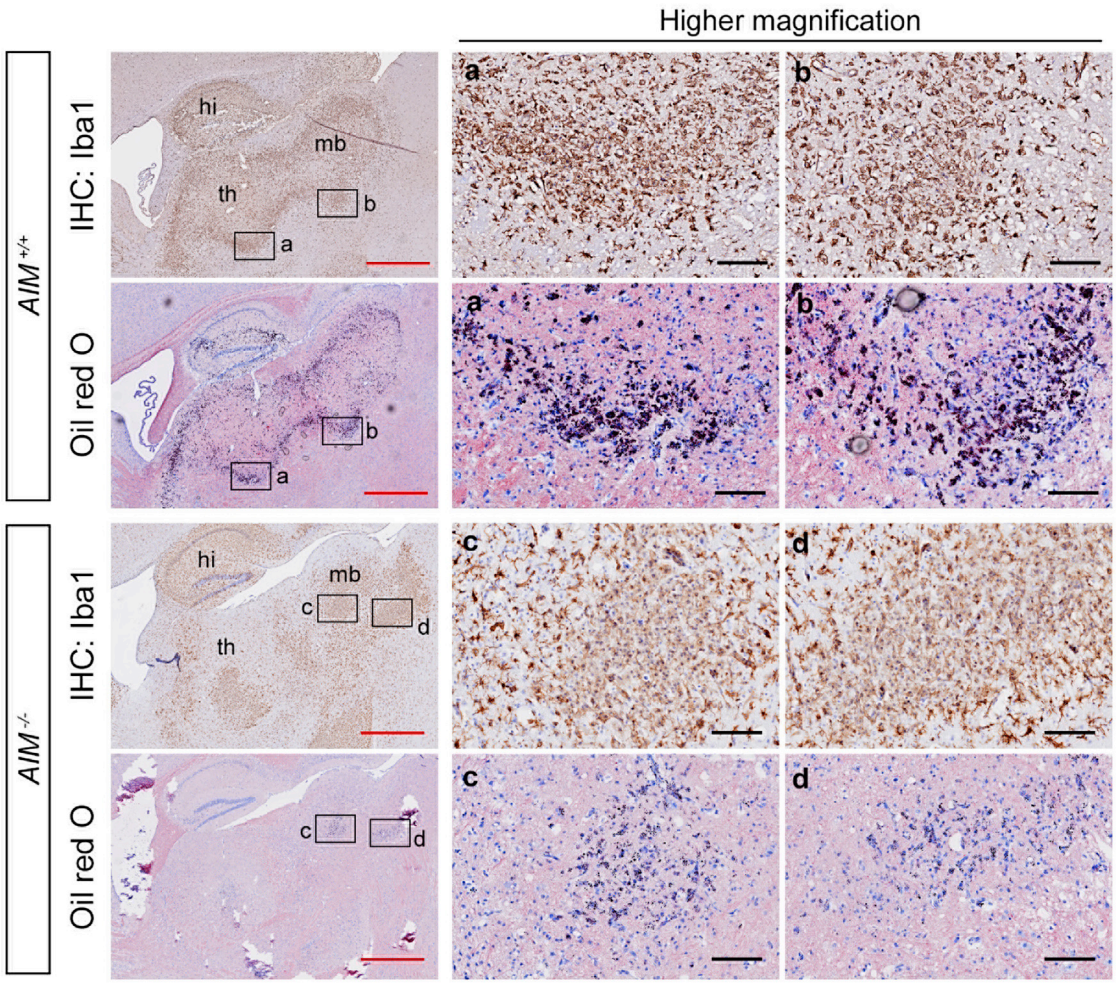

Figure 2. Inefficient engulfment of dead cell debris by infiltrating macrophages at the infarct area in the absence of AIM

Serial frozen sections from wild-type and *AIM*$^{-/-}$ brains on day 7 post-MCAO were stained for oil red O and Iba1. Many Iba1-positive macrophages at the infarcted corpus striatum region are positive for oil red O (violet signals) in wild-type mice, whereas they are largely negative for oil red O in *AIM*$^{-/-}$ mice. Red bars, 1 mm; black bars, 100 μm.

In accordance with the reduction of DAMPs, the mRNA levels of the inflammatory cytokines expressed in CD11b^{+} macrophages/myeloid cells infiltrating the infarcted brain on day 4 after MCAO were reduced by rAIM injection in *AIM*$^{-/-}$ and/or wild-type mice, suggesting that AIM decreased inflammation in the infarcted region (Figure 3C). Without rAIM injection, however, only a certain, and not significant, increase in cytokine mRNA levels was observed in *AIM*$^{-/-}$ mice compared with wild-type mice (Figure 3C), in line with the low level of brain AIM in wild-type mice before day 7 (Figure 1A).

AIM improved the prognosis of ischemic stroke

In parallel with the volume of DAMPs and inflammatory states in the brain, the mortality on day 7 after MCAO was higher in *AIM*$^{-/-}$ mice compared with wild-type mice, and it was profoundly reduced by daily injection of *AIM*$^{-/-}$ mice with rAIM (0.5 mg/mouse) (Figure 4A). No wild-type mice died after MCAO when they were injected with an even smaller amount (0.1 mg/mouse) of rAIM (Figure 4A). The difference in mortality between wild-type and *AIM*$^{-/-}$ mice became obvious concurrently with the increase in brain *AIM* mRNA levels in wild-type mice (Figure 1A). Similarly, neurologic deficits were exacerbated in *AIM*$^{-/-}$ mice, which were again improved by rAIM injection (Figure 4B). Note that the performance of MCAO was consistently successful, as judged by the comparable reduction of blood flow in the middle cerebral artery during MCAO (Figure S4). Thus, intravenous administration of rAIM during the acute phase of stroke effectively improved the post-stroke prognosis therapeutically. However, the rAIM injection did not improve survival and neurologic scores in *AIM*$^{-/-}$ mice to the levels in wild-type mice at day 7, despite the better suppression of inflammation in rAIM-injected *AIM*$^{-/-}$ mice than in wild-type mice at day 4 (Figure 3C). This discrepancy is explained by the lower amount of AIM accumulated at the infarcted area in rAIM-injected *AIM*$^{-/-}$ mice than in wild-type mice at day 7 (Figure 4C). It is worth reemphasizing that the endogenous AIM

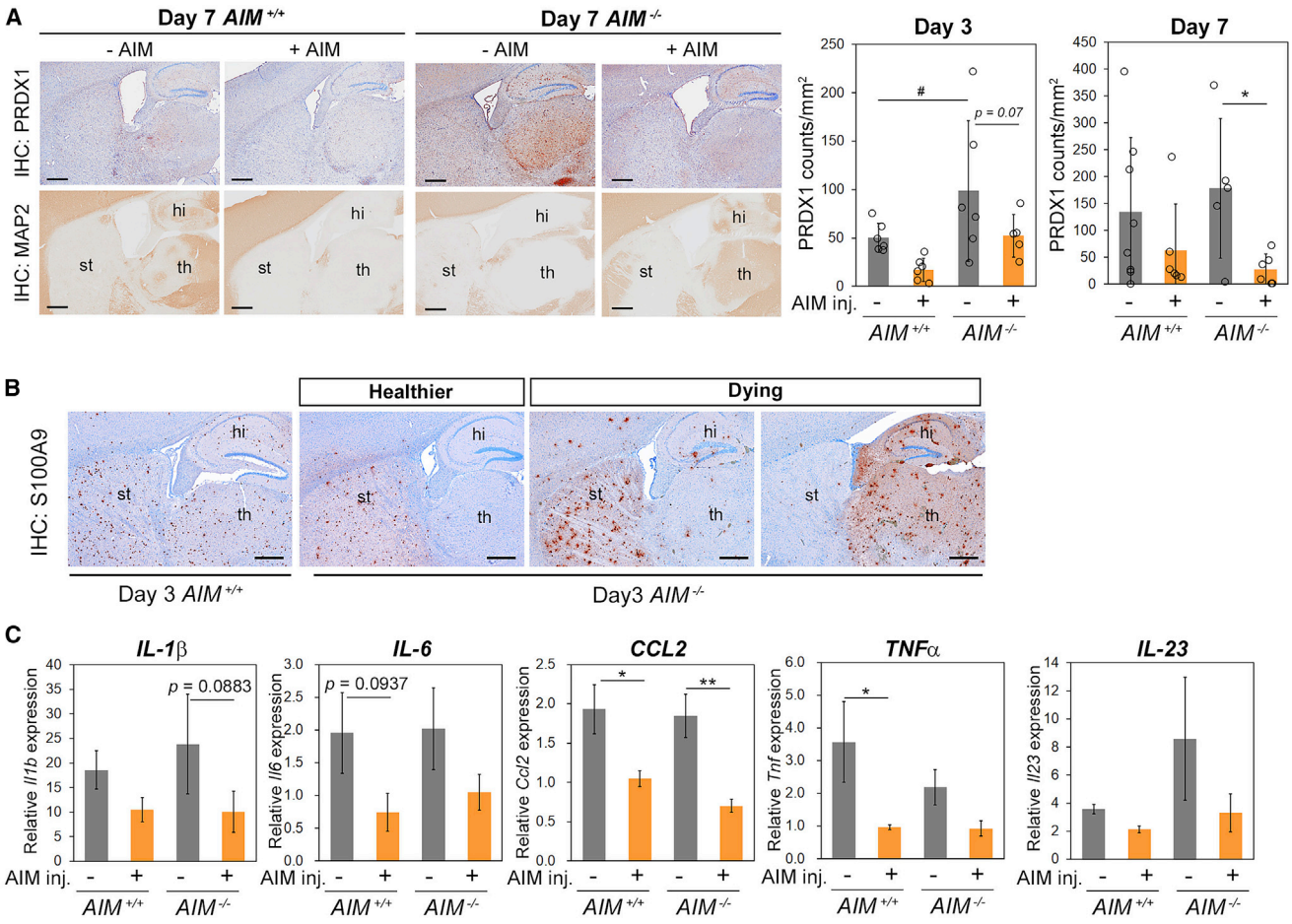

Figure 3. AIM suppressed brain inflammation by reducing DAMPs

(A) The brain specimens from wild-type ($AIM^{+/+}$) and $AIM^{-/-}$ mice with or without rAIM injection (0.5 mg daily from day 1 after MCAO) on days 3 and 7 after MCAO were stained for PRDX1, HMGB1, or S100A9, as well as with hematoxylin to identify nuclei. Representative photos of PRDX1 (upper panels) and MAP2 (lower panels) staining on day 7 post-MCAO are presented. Bars, 500 μm. The number of positive signals for PRDX1 (brown signals) within the MAP2-negative region that were not co-localized with the hematoxylin signals was counted and normalized by the area (mm^2) of MAP2-negative region. n = 5–8. Statistics: multi-way ANOVA followed by Bonferroni's post hoc test. *p < 0.05 (comparison between with and without AIM injection); #p < 0.05 ($AIM^{+/+}$ vs. $AIM^{-/-}$). The results for HMGB1 and S100A9 are presented in Figure S3. st, striatum; hi, hypothalamus; th, thalamus.

(B) S100A9 staining on day 3 in two dying and a healthier $AIM^{-/-}$ mice, as well as a wild-type mouse. The brains from dying $AIM^{-/-}$ mice showed a markedly larger number of intense signals than the other healthier $AIM^{-/-}$ mice or wild-type mice on day 3. st, striatum; hi, hypothalamus; th, thalamus. Note that the reduction of blood flow in the middle cerebral artery by MCAO was comparable in mice, confirming that the severity of MCAO was not different among the tested mice. Bars, 500 μm.

(C) qPCR analysis of the mRNA levels of inflammatory cytokines using RNA from $CD11^+$ macrophages/myeloid cells isolated from the infarcted brain in wild-type and $AIM^{-/-}$ with or without rAIM injection (0.5 mg daily from day 1 after MCAO) on day 4 after MCAO. Relative values to those in $CD11^+$ cells isolated from healthy brain are presented. n = 4–6 each. Average values ± SEM are presented. Statistics: multi-way ANOVA followed by Bonferroni's post hoc test. *p < 0.05 and **p < 0.01.

levels in the affected brain were markedly lower at day 3 compared with day 7 in post-infarcted wild-type mice (Figure 1A). Consistent with the lower level of intracerebral AIM, the mRNA levels of inflammatory M1 macrophage genes, *Il-1β*, *Il-6*, and *NOS2* (*iNOS*) in the affected brain were higher in rAIM-injected $AIM^{-/-}$ mice than wild-type mice at day 7 (Figure 4D).

All these results suggest the hypothesis that AIM facilitates the removal of regional dead cell debris or DAMPs, or even both, which results in a decrease in post-stroke sterile inflammation, thereby improving the prognosis.

Association of AIM with DAMPs and their binding modes

To test this hypothesis from the mechanistic view of AIM action, we first determined whether AIM binds directly to DAMPs, similar to its binding to dead cell debris, using an ELISA-based system. As shown in Figure 5A, AIM bound to PRDX1, S100A9, and HMGB1, as well as many other DAMPs in a dose-dependent manner. Consistent with this result, at the infarcted area in mice, the close interaction between AIM and PRDX1 as a representative of DAMPs was observed when assessed using proximity ligation assay (Figure S5A). We also tested the binding of AIM and DAMPs biochemically. After an incubation of mouse

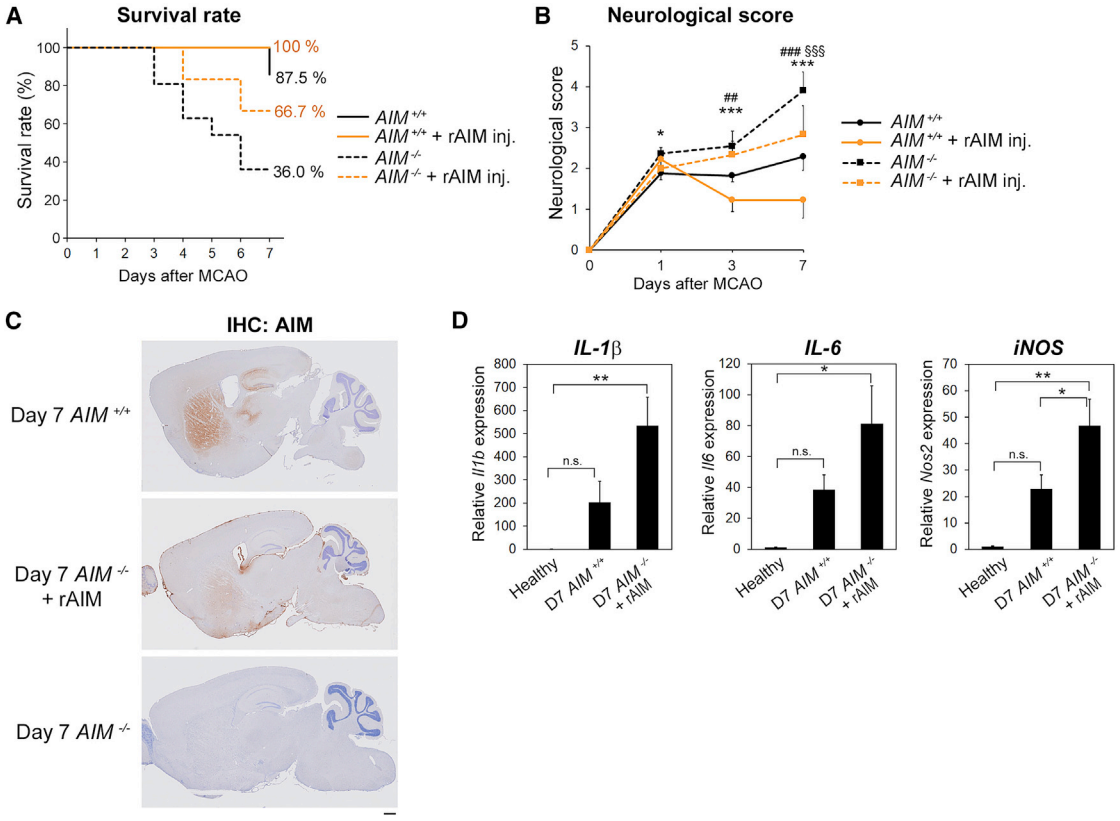

Figure 4. AIM improved the post-stroke prognosis

(A) Survival of wild-type, *AIM*$^{-/-}$, rAIM (0.5 mg)-injected *AIM*$^{-/-}$, and rAIM (0.1 mg)-injected wild-type mice after MCAO. n = 38 (wild-type), 21 (*AIM*$^{-/-}$), 9 (wild-type + rAIM injection), and 12 (*AIM*$^{-/-}$ + rAIM injection). rAIM was injected intravenously daily from day 1. Statistical significance of survival during the 7 days after MCAO was assessed using the generalized Wilcoxon test. p = 0.0000347 in wild-type mice versus *AIM*$^{-/-}$ mice; p = 0.0780 in *AIM*$^{-/-}$ mice with rAIM versus *AIM*$^{-/-}$ mice without rAIM injection.

(B) Neurologic scores in the four groups of mice as in (A). n = 17 (wild-type), 11 (*AIM*$^{-/-}$), 9 (wild-type + rAIM injection), and 6 (*AIM*$^{-/-}$ + rAIM injection). Mean values ± SEM are presented. Statistics: multi-way repeated-measures ANOVA followed by Bonferroni's post hoc test. *p < 0.05 and ***p < 0.001 (wild-type versus *AIM*$^{-/-}$), $^{\#\#}$p < 0.01 and $^{\#\#\#}$p < 0.001 (wild-type versus wild-type + rAIM injection), and §§§p < 0.001 (*AIM*$^{-/-}$ versus *AIM*$^{-/-}$ + rAIM injection).

(C) Immunohistochemistry for AIM in wild-type, *AIM*$^{-/-}$ + rAIM injection, and *AIM*$^{-/-}$ (non-injected) mouse at d days 7 after MCAO. Representative photos are presented. Similar results were obtained in three groups of different specimens. Bar, 500 μm.

(D) qPCR analysis of the mRNA levels of inflammatory M1 macrophage genes in the infarcted brain in wild-type and *AIM*$^{-/-}$ with or without rAIM injection (0.5 mg daily from day 1 after MCAO) on day 7 after MCAO. Relative values to those in healthy brain are presented. n = 4 each. Average values ± SEM are presented. Statistics: one-way ANOVA followed by Bonferroni's post hoc test. *p < 0.05 and **p < 0.01.

rAIM with PRDX1, S100A, or HMGB1, the association of AIM and each DAMP was evaluated using immunoblotting in non-reducing condition using an anti-AIM antibody. As shown in Figure S5B, in addition to the signal corresponding to the 1:1 association in size, several signals of larger molecular weights were observed, suggesting that multiple number of AIM and the DAMP formed a complex. Although AIM possessed single free cysteine residue, it is likely that DAMPs harbor multiple free cysteines derived from the collapsed internal disulfide bonds, which may allow to form larger complexes containing multiple numbers of AIM and the DAMP. The possible number of AIM and the DAMP involved in the complex, estimated by the molecular weight, is indicated. The relatively lower binding efficiency of HMGB1 to mouse AIM is consistent with the ELISA data (Figure 5A).

Most DAMPs are negatively charged (Uchida, 2014; Knoops et al., 2018), which may enable their binding to AIM via charge-based interactions, similar to the association of AIM with dead cell debris (Arai et al., 2016; Tomita et al., 2017). To address the involvement of charge-based interactions using the carboxyl terminus of AIM in its binding with DAMPs, as with debris, we examined the association of DAMPs with a mutant mouse AIM that lacks the carboxyl domain (ΔSRCR3) (Yamazaki et al., 2016; Hiramoto et al., 2018). As expected, ΔSRCR3 showed essentially no binding to any DAMP (Figure 5B). In addition, the association between AIM and DAMPs was significantly reduced in the presence of high doses of NaCl, which interrupts the charge-based interactions of two molecules (Figure 5C).

Intriguingly, the binding of AIM to most DAMPs was also disrupted in the presence of a reducing agent, Tris(2-carboxyethyl)phosphine (TCEP) (Figure 5D), suggesting the additional involvement of disulfide bonds. As the solitary cysteine residue in the SRCR2 domain is the only available site for disulfide

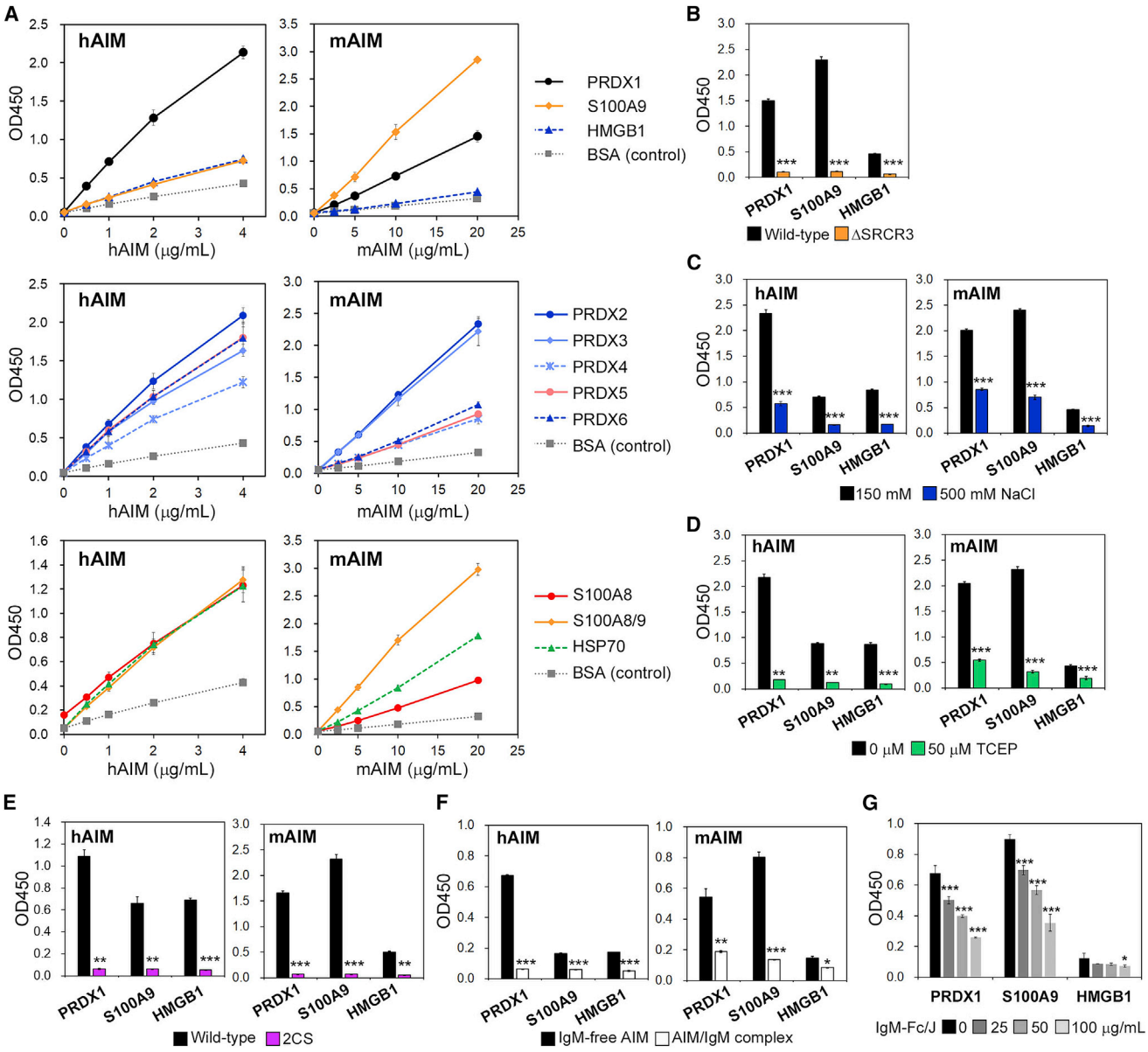

Figure 5. AIM bound to DAMPs through charge-based interactions and disulfide bond formation

(A) *In vitro* binding assay of AIM to various DAMPs. The binding abilities of different concentrations of human or mouse AIM to PRDX1, HMGB1, S100A9, and bovine serum albumin (BSA) as a control (coated on the plate at 2 μg/mL) are presented. The assay was performed in triplicate, and average values ± SD are presented.

(B and C) The binding abilities of mouse ΔSRCR3 mutant (B) or (C) wild-type human AIM (4 μg/mL each) and mouse AIM (20 μg/mL each) in the presence of 150 mM (physiological) or 500 mM (excess) of NaCl to PRDX1, HMGB1, and S100A9. In the presence of excess NaCl, binding was largely diminished.

(D and E) The binding abilities of human AIM (4 μg/mL each) and mouse wild-type AIM (20 μg/mL) to the indicated DAMPs in the presence of 50 μM TCEP (D) or (E) human and mouse 2CS mutant to PRDX1, HMGB1, and S100A9. Binding was again diminished.

(F) The binding ability of recombinant human and mouse AIM/IgM-Fc pentamer complexes to DAMPs performed as in (A). Binding was diminished.

(G) Binding of mouse AIM to DAMPs was impaired by mouse IgM-Fc pentamer in a dose-dependent manner.

In (B)–(G), the assay was performed in triplicate and the average values are presented. Statistics: Welch's t test (B–F), one-way ANOVA followed by Bonferroni's post hoc test, *$p < 0.05$, **$p < 0.01$, and ***$p < 0.001$ (versus control).

bond formation with a different molecule (Miyazaki et al., 1999; Hiramoto et al., 2018), we prepared another AIM mutant in which the cysteine was substituted to serine (2CS) and assessed its binding to DAMPs. As shown in Figure 5E, the 2CS mutant lost the ability to bind to all DAMPs examined. Note that the antibody used to detect the DAMP-bound AIM in this experiment recognized wild-type AIM, ΔSRCR3, and 2CS comparably (Figure S5C). Altogether, it is likely that AIM associates with DAMPs

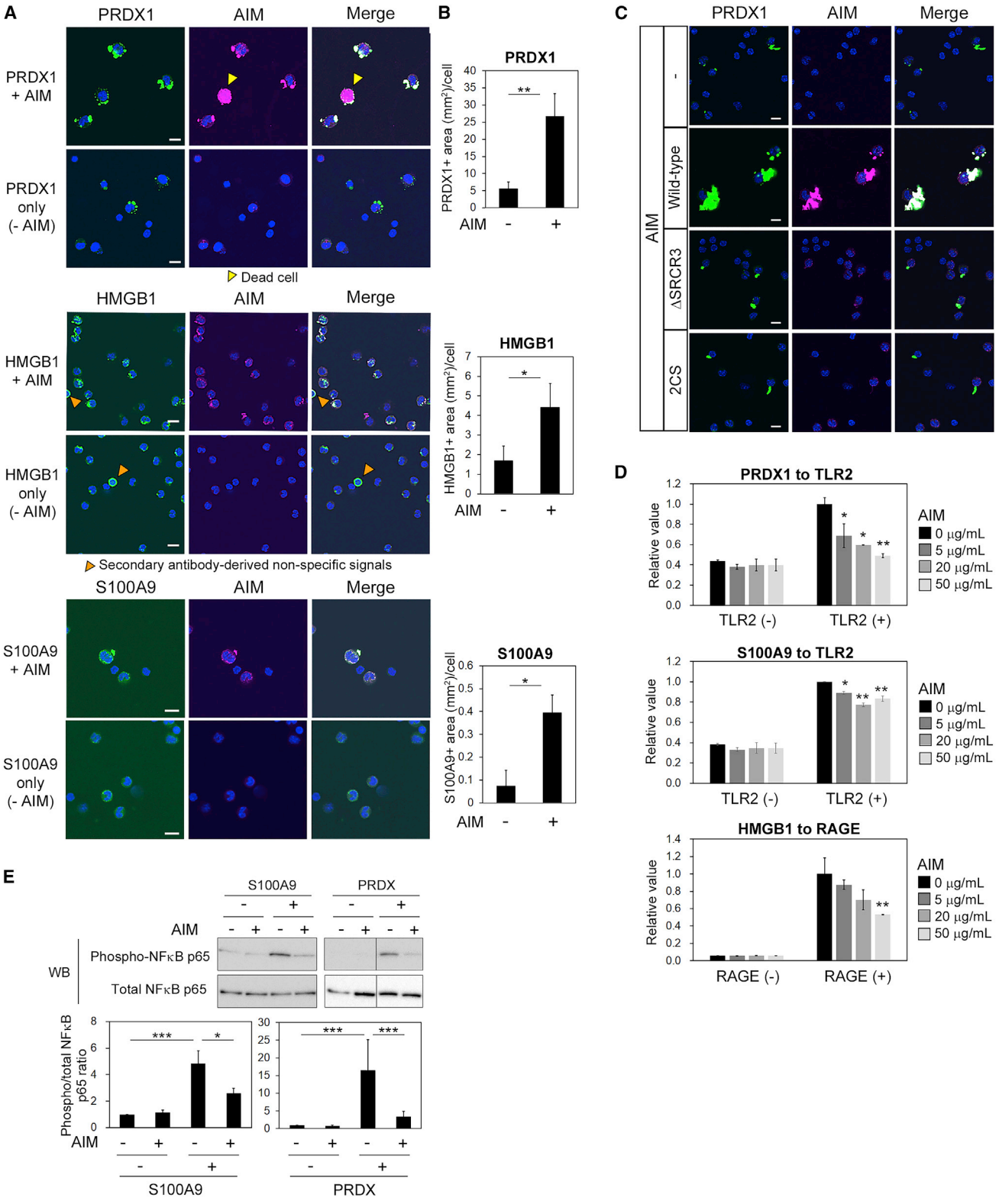

Figure 6. Attenuation of DAMP-mediated pro-inflammatory responses by AIM

(A) Peritoneal macrophages isolated from *AIM*$^{-/-}$ mice were challenged with PRDX1, HMGB1, and S100A9 on a chamber slide in the presence or absence of rAIM. After incubation for 10 min, the cells were fixed and stained for each DAMP (green), AIM (magenta), and nuclei (blue) and analyzed under a florescence

(legend continued on next page)

stably using two independent binding modes: charge-based interactions and disulfide bond formation.

Either coincidentally or necessarily, these two binding sites are also used for the association of AIM with IgM pentamer, as we reported previously (Hiramoto et al., 2018). This fact suggests that AIM may lose its ability to bind to DAMPs when it associates with IgM pentamer. Supporting this hypothesis, AIM-IgM complexes exhibited largely no binding to DAMPs (Figure 5F). Furthermore, the presence of AIM-free IgM pentamer competitively interfered with the binding of AIM to DAMPs in a dose-dependent manner (Figure 5G). Therefore, IgM-bound AIM is functionally inactive in terms of binding to DAMPs.

AIM enhanced the phagocytic removal of DAMPs and also neutralized DAMPs

Having observed the direct binding of AIM to DAMPs, we challenged macrophages with PRDX1, HMGB1, and S100A9 *in vitro* in the presence or absence of rAIM and assessed the influence of AIM association on the capture of DAMPs by macrophages under a fluorescence microscope. As shown in Figure 6A, AIM was highly co-localized with all DAMPs, corroborating the binding data obtained with ELISA (Figure 5A; control photos are presented in Figure S6A). Moreover, the volume of PRDX1, HMGB1, or S100A9 present on the cell surface or within the cells was significantly increased in the presence of rAIM, suggesting that AIM enhances the capture of DAMPs by macrophages (Figure 6B). Interestingly, AIM association highly induced the aggregation of PRDX1 (Figure 6C), which was reminiscent of a similar observation for AIM-induced bacterial aggregation (Sarrias et al., 2005). Notably, neither ΔSRCR3 nor 2CS AIM mutant, both of which had no binding to DAMPs (Figures 5B and 5E), induced PRDX1 aggregation (Figure 6C). rAIM did not induce such aggregation for HMGB1 or S100A9, though the reason is unknown. However, this result is consistent with the observation that the decrease in PRDX1 by AIM at the infarcted region *in vivo* was more apparent than in HMGB1 or S100A9 (presented in Figure 3A), as larger molecules are more readily engulfed by phagocytes (Aderem and Underhill, 1999; Sarrias et al., 2005; Canton et al., 2013). The HMGB1 or PRDX1 and the associated rAIM engulfed by the *AIM*$^{-/-}$ peritoneal macrophages were co-localized within the LAMP2-positive lysosomes and thereafter disappeared (Figure S6B). Internalization of DAMPs together with AIM by macrophages was also corroborated by flow cytometry (Figure S6C).

Importantly, AIM association interfered with the binding of PRDX1 and HMGB1 to the inflammatory receptors TLR2 and RAGE, when assessed using an ELISA-based assay (Figure 6D). This result suggests that AIM competitively impeded the charge-based interactions of some DAMPs to TLR and RAGE, in addition to the enhancement of DAMP internalization. It is likely that such AIM actions, namely, enhancement of phagocytic DAMP removal and neutralization of DAMPs, overall result in diminishment of the inflammatory activity of DAMPs. As a representative, the ability of PRDX and S100 to activate NF-κB in macrophage cells was significantly reduced by rAIM (Figure 6E; whole blots are presented in Figure S7).

Conclusion and perspectives

Our present findings strongly support the possibility of developing AIM-based therapy against ischemic stroke. It is worth re-emphasizing that AIM efficiently suppressed sterile inflammation in the infarcted brain by directly targeting DAMPs. Unlike the binding of DAMPs with TLRs and RAGE, which is mediated mainly by charge-based interactions, the additional formation of a disulfide bond increased the intensity and stability of the association of AIM with DAMPs. This strong association must be advantageous in competitively reducing DAMP binding to TLRs and RAGE, thereby successfully decreasing the inflammatory threat of DAMPs. As a consequence of attenuating the action of DAMPs, the therapeutic effect of rAIM against ischemic stroke was obvious. Impaired DAMP clearance and the resulting acceleration of the deleterious effects of stroke in *MafB*$^{-/-}$ mice reported by Yoshimura's group (Shichita et al., 2017) might be due partially to the inefficient production of AIM in the infarcted brain (Figure 1C).

The amount of rAIM that reaches brain tissue could be different in individuals according to the level of damage to the BBB (Choi et al., 2016; Zou et al., 2015). Indeed, the amount of AIM accumulating at the infarcted region was less in *AIM*$^{-/-}$ mice daily injected with rAIM than in wild-type mice (Figure 4C), and thus overall survival and neurologic scores were better in wild-type mice than rAIM-injected *AIM*$^{-/-}$ mice at day 7 (Figures 4A and 4B). Future development of optimized or modified AIM that can effectively transit from the blood to the brain regardless of BBB damage will achieve more efficient and steadier therapeutic efficacy for ischemic stroke. In addition to the therapeutic effect of AIM during the acute phase of stroke presented in the present study, it is possible that the rapid and efficient reduction

confocal microscope. White areas indicate colocalization of DAMPs and AIM. Attachment of rAIM to some dead cells is also observed (yellow arrows). Non-specific signals (background) derived by secondary antibody developed in HMGB1 staining (orange arrows). Bar, 10 μm.

(B) The volume of each PRDX1, HMGB1, or S100A9 present at the cell surface and intracellulary was determined using software Halo and presented in the graph. Values are averages of the results from three experiments (n = 4–13). Statistics: Welch's t test. *p < 0.05 and **p < 0.01.

(C) Induction of PRDX1 aggregation by AIM (wild-type), ΔSRCR3 mutant, and 2CS mutant. Bar, 10 μm.

(D) Binding of PRDX1 and S100A9 to TLR2 and HMGB1 to RAGE in the presence of various concentrations of rAIM. The values in the absence of TLR2 or RAGE are also presented as control. rAIM reduced the ability of PRDX1 and S100A9 to bind to TLR2 and HMGB1 to RAGE in a dose-dependent manner. The assay was performed in triplicate and the average values are presented. Statistics: one-way ANOVA followed by Bonferroni's post hoc test. *p < 0.05 and **p < 0.01 (comparison between 0 μg/mL of rAIM and each concentration of rAIM).

(E) RAW264.1 mouse macrophage cells were incubated with mouse PRDX or S100A9 for 30 min at 37°C in the presence or absence of rAIM. Thereafter, the cells were harvested, and the cell lysates were analyzed for phosphorylation (indicating NF-κB activation) by immunoblotting. The intensity of the signals was quantified and presented in the graphs. Values represent intensity of the phosphorylated NF-κB p65 relative to that of total NF-κB p65. The presence of rAIM decreased NF-κB phosphorylation. Statistics: two-way ANOVA followed by Bonferroni's post hoc test. *p < 0.05 and ***p < 0.001. The whole blots are presented in Figure S7.

of sterile inflammation by AIM in the infarcted region might advance regional post-injury neurogenesis, which raises our expectation for a beneficial effect of AIM also during recovery from stroke. Further studies focusing on later days post-stroke might expand the therapeutic applicability of AIM to multiple phases of ischemic stroke.

In the normal condition, AIM associates with pentameric IgM in the blood, which protects AIM from renal excretion and maintains high levels of blood AIM (Arai et al., 2013, 2016; Tomita et al., 2017). Although we know that AIM needs to dissociate from IgM pentamer to become functionally active (Arai et al., 2016; Sugisawa et al., 2016; Koyama et al., 2018), the precise machinery by which its association with IgM pentamer inactivates AIM remained unclear. This question was solved by our present finding that AIM uses the same sites to bind to DAMPs and IgM pentamer. Using electron microscopy, we recently found that pentameric IgM forms a ''one-piece missing hexamer'' and that AIM fits stably in the gap through a disulfide bond at one side of the gap and charge-based interactions at the other side (Hiramoto et al., 2018). Importantly, the shape and size of the gap need to be strictly appropriate for the formation of both binding bridges (Hiramoto et al., 2018). From this aspect, it is plausible that DAMPs may also have or develop a similar gap structure into which AIM fits. Additional analysis from the structural viewpoint is required to understand the precise binding mode between AIM and DAMPs.

In conclusion, our data suggest the strong therapeutic applicability of AIM to ischemic stroke and, in addition, clarify new functional aspects of AIM.

STAR★METHODS

Detailed methods are provided in the online version of this paper and include the following:

- KEY RESOURCES TABLE
- RESOURCE AVAILABILITY
  - Lead contact
  - Materials availability
  - Data and code availability
- EXPERIMENTAL MODEL AND SUBJECT DETAILS
  - Animals
  - Primary cell cultures and cell lines
- METHOD DETAILS
  - Induction of ischemic stroke (MCAO)
  - Antibodies and reagents
  - DAMPs and related proteins
  - CD11b^{+} cell isolation from brain
  - EILSA for AIM
  - Production and purification of rAIM and related proteins
  - Evaluation of binding efficiency of AIM to DAMPs
  - Proximity ligation assay (PLA)
  - *In vitro* evaluation of DAMPs captures by macrophage
  - Flowcytometry
  - NFκB activation assay
  - Histology
  - Quantification of DAMPs in brain
  - Evaluation of neurologic deficits (neurologic score)
  - Quantitative PCR assay
- QUANTIFICATION AND STATISTICAL ANALYSIS

SUPPLEMENTAL INFORMATION

Supplemental information can be found online at https://doi.org/10.1016/j.celrep.2021.109693.

ACKNOWLEDGMENTS

We thank Drs. K. Kurokawa, K. Tanabe, K. Toyota, and T. Ago for helpful advice and discussion; Drs. S. Takahashi and M. Hamada for providing Lysm-Cre;*MafB*$^{-/-}$ mice; Dr. S. Shichita and T. Nonomura for advice about MCAO; Dr. R. Suzuki for help with rAIM production; K. Yasuda for help with statistical analysis of the data; E. Hiramoto, A. Nishijima, T. Yoshida, and Y. Yoshikawa for technical assistance; and K. Ohkubo and Y. Noguchi for helpful technical advice on histology. This work was supported by AMED-CREST (JP18gm0610009) and AMED-LEAP (JP20gm0010006), Japan Agency for Medical Research Development (to T.M.); Japan Society for the Promotion of Science (JSPS) KAKENHI Grant-in-Aid for Scientific Research (B) (grant 20H03446 to S.A., grant 19K16535 to N.M., and grant 20K16213 to K.T.); and the Takeda Science Foundation (to S.A.).

AUTHOR CONTRIBUTIONS

N.M., K.T., and A.O. carried out major experiments; mainly, N.M. performed animal experiments, histologic analysis, and qPCR, K.T. contributed to tissue staining and assessments of histologic data, and A.O. performed many MCAO procedures. H.A. performed binding assay for AIM and DAMPs, as well as biochemical experiments. A.H. performed tissue staining. Z.L. performed qPCR. C.-T.W. contributed to animal experiments. S.A. performed all cell-based experiments, including the analysis of DAMP internalization. S.A. and T.M. designed experiments. T.M. supervised the whole study and wrote the paper.

DECLARATION OF INTERESTS

The authors declare no competing interests.

INCLUSION AND DIVERSITY

We worked to ensure diversity in experimental samples through the selection of the cell lines.

Received: January 22, 2021
Revised: July 1, 2021
Accepted: August 18, 2021
Published: September 14, 2021

REFERENCES

Aderem, A., and Underhill, D.M. (1999). Mechanisms of phagocytosis in macrophages. Annu. Rev. Immunol. *17*, 593–623.

Alim, I., Caulfield, J.T., Chen, Y., Swarup, V., Geschwind, D.H., Ivanova, E., Seravalli, J., Ai, Y., Sansing, L.H., Ste Marie, E.J., et al. (2019). Selenium drives a transcriptional adaptive program to block ferroptosis and treat stroke. Cell *177*, 1262–1279.e25.

Arai, S., and Miyazaki, T. (2018). A scavenging system against internal pathogens promoted by the circulating protein apoptosis inhibitor of macrophage (AIM). Semin. Immunopathol. *40*, 567–575.

Arai, S., Maehara, N., Iwamura, Y., Honda, S., Nakashima, K., Kai, T., Ogishi, M., Morita, K., Kurokawa, J., Mori, M., et al. (2013). Obesity-associated autoantibody production requires AIM to retain the immunoglobulin M immune complex on follicular dendritic cells. Cell Rep. *3*, 1187–1198.

Arai, S., Kitada, K., Yamazaki, T., Takai, R., Zhang, X., Tsugawa, Y., Sugisawa, R., Matsumoto, A., Mori, M., Yoshihara, Y., et al. (2016). Apoptosis inhibitor of macrophage protein enhances intraluminal debris clearance and ameliorates acute kidney injury in mice. Nat. Med. *22*, 183–193.

Bonventre, J.V., and Yang, L. (2011). Cellular pathophysiology of ischemic acute kidney injury. J. Clin. Invest. *121*, 4210–4221.

Canton, J., Neculai, D., and Grinstein, S. (2013). Scavenger receptors in homeostasis and immunity. Nat. Rev. Immunol. *13*, 621–634.

Chamorro, Á., Dirnagl, U., Urra, X., and Planas, A.M. (2016). Neuroprotection in acute stroke: targeting excitotoxicity, oxidative and nitrosative stress, and inflammation. Lancet Neurol. *15*, 869–881.

Chen, G.Y., and Nuñez, G. (2010). Sterile inflammation: sensing and reacting to damage. Nat. Rev. Immunol. *10*, 826–837.

Choi, K.H., Kim, H.S., Park, M.S., Lee, E.B., Lee, J.K., Kim, J.T., Kim, J.H., Lee, M.C., Lee, H.J., and Cho, K.H. (2016). Overexpression of caveolin-1 attenuates brain edema by inhibiting tight junction degradation. Oncotarget *7*, 67857–67867.

David, S., and Kroner, A. (2011). Repertoire of microglial and macrophage responses after spinal cord injury. Nat. Rev. Neurosci. *12*, 388–399.

Dayon, L., Turck, N., Garcí-Berrocoso, T., Walter, N., Burkhard, P.R., Vilalta, A., Sahuquillo, J., Montaner, J., and Sanchez, J.C. (2011). Brain extracellular fluid protein changes in acute stroke patients. J. Proteome Res. *10*, 1043–1051.

Engel, S., Schluesener, H., Mittelbronn, M., Seid, K., Adjodah, D., Wehner, H.D., and Meyermann, R. (2000). Dynamics of microglial activation after human traumatic brain injury are revealed by delayed expression of macrophage-related proteins MRP8 and MRP14. Acta Neuropathol. *100*, 313–322.

Gülke, E., Gelderblom, M., and Magnus, T. (2018). Danger signals in stroke and their role on microglia activation after ischemia. Ther. Adv. Neurol. Disord. *11*, 1756286418774254.

Hamada, M., Nakamura, M., Tran, M.T., Moriguchi, T., Hong, C., Ohsumi, T., Dinh, T.T., Kusakabe, M., Hattori, M., Katsumata, T., et al. (2014). MafB promotes atherosclerosis by inhibiting foam-cell apoptosis. Nat. Commun. *5*, 3147.

Hayakawa, K., Qiu, J., and Lo, E.H. (2010). Biphasic actions of HMGB1 signaling in inflammation and recovery after stroke. Ann. N Y Acad. Sci. *1207*, 50–57.

Hiramoto, E., Tsutsumi, A., Suzuki, R., Matsuoka, S., Arai, S., Kikkawa, M., and Miyazaki, T. (2018). The IgM pentamer is an asymmetric pentagon with an open groove that binds the AIM protein. Sci. Adv. *4*, eaau1199.

Hudson, B.I., and Lippman, M.E. (2018). Targeting RAGE signaling in inflammatory disease. Annu. Rev. Med. *69*, 349–364.

Humphreys, B.D., Valerius, M.T., Kobayashi, A., Mugford, J.W., Soeung, S., Duffield, J.S., McMahon, A.P., and Bonventre, J.V. (2008). Intrinsic epithelial cells repair the kidney after injury. Cell Stem Cell *2*, 284–291.

Iadecola, C., and Anrather, J. (2011). The immunology of stroke: from mechanisms to translation. Nat. Med. *17*, 796–808.

Jiang, S.X., Lertvorachon, J., Hou, S.T., Konishi, Y., Webster, J., Mealing, G., Brunette, E., Tauskela, J., and Preston, E. (2005). Chlortetracycline and demeclocycline inhibit calpains and protect mouse neurons against glutamate toxicity and cerebral ischemia. J. Biol. Chem. *280*, 33811–33818.

Kawabori, M., Kacimi, R., Kauppinen, T., Calosing, C., Kim, J.Y., Hsieh, C.L., Nakamura, M.C., and Yenari, M.A. (2015). Triggering receptor expressed on myeloid cells 2 (TREM2) deficiency attenuates phagocytic activities of microglia and exacerbates ischemic damage in experimental stroke. J. Neurosci. *35*, 3384–3396.

Knoops, B., Becker, S., Poncin, M.A., Glibert, J., Derclaye, S., Clippe, A., and Alsteens, D. (2018). Specific interactions measured by AFM on living cells between peroxiredoxin-5 and TLR4: relevance for mechanisms of innate immunity. Cell Chem. Biol. *25*, 550–559.e3.

Knowland, D., Arac, A., Sekiguchi, K.J., Hsu, M., Lutz, S.E., Perrino, J., Steinberg, G.K., Barres, B.A., Nimmerjahn, A., and Agalliu, D. (2014). Stepwise recruitment of transcellular and paracellular pathways underlies blood-brain barrier breakdown in stroke. Neuron *82*, 603–617.

Kono, H., and Rock, K.L. (2008). How dying cells alert the immune system to danger. Nat. Rev. Immunol. *8*, 279–289.

Koyama, N., Yamazaki, T., Kanetsuki, Y., Hirota, J., Asai, T., Mitsumoto, Y., Mizuno, M., Shima, T., Kanbara, Y., Arai, S., et al. (2018). Activation of apoptosis inhibitor of macrophage is a sensitive diagnostic marker for NASH-associated hepatocellular carcinoma. J. Gastroenterol. *53*, 770–779.

Kumar, S., Ingle, H., Prasad, D.V., and Kumar, H. (2013). Recognition of bacterial infection by innate immune sensors. Crit. Rev. Microbiol. *39*, 229–246.

Kurokawa, J., Arai, S., Nakashima, K., Nagano, H., Nishijima, A., Miyata, K., Ose, R., Mori, M., Kubota, N., Kadowaki, T., et al. (2010). Macrophage-derived AIM is endocytosed into adipocytes and decreases lipid droplets via inhibition of fatty acid synthase activity. Cell Metab. *11*, 479–492.

Kusaba, T., Lalli, M., Kramann, R., Kobayashi, A., and Humphreys, B.D. (2014). Differentiated kidney epithelial cells repair injured proximal tubule. Proc. Natl. Acad. Sci. U S A *111*, 1527–1532.

Land, W.G. (2020). Use of DAMPs and SAMPs as therapeutic targets or therapeutics: a note of caution. Mol. Diagn. Ther. *24*, 251–262.

Lane, M.A., and Bailey, S.J. (2005). Role of retinoid signalling in the adult brain. Prog. Neurobiol. *75*, 275–293.

Liu, Q., Jin, W.-N., Liu, Y., Shi, K., Sun, H., Zhang, F., Zhang, C., Gonzales, R.J., Sheth, K.N., La Cava, A., and Shi, F.-D. (2017). Brain ischemia suppresses immunity in the periphery and brain via different neurogenic innervations. Immunity *46*, 474–487.

Maehara, N., Arai, S., Mori, M., Iwamura, Y., Kurokawa, J., Kai, T., Kusunoki, S., Taniguchi, K., Ikeda, K., Ohara, O., et al. (2014). Circulating AIM prevents hepatocellular carcinoma through complement activation. Cell Rep. *9*, 61–74.

Medzhitov, R. (2008). Origin and physiological roles of inflammation. Nature *454*, 428–435.

Miyazaki, T., Hirokami, Y., Matsuhashi, N., Takatsuka, H., and Naito, M. (1999). Increased susceptibility of thymocytes to apoptosis in mice lacking AIM, a novel murine macrophage-derived soluble factor belonging to the scavenger receptor cysteine-rich domain superfamily. J. Exp. Med. *189*, 413–422.

Oxley, T.J., Mocco, J., Majidi, S., Kellner, C.P., Shoirah, H., Singh, I.P., De Leacy, R.A., Shigematsu, T., Ladner, T.R., Yaeger, K.A., et al. (2020). Large-vessel stroke as a presenting feature of COVID-19 in the young. N. Engl. J. Med. *382*, e60.

Passey, R.J., Williams, E., Lichanska, A.M., Wells, C., Hu, S., Geczy, C.L., Little, M.H., and Hume, D.A. (1999). A null mutation in the inflammation-associated S100 protein S100A8 causes early resorption of the mouse embryo. J. Immunol. *163*, 2209–2216.

Qiu, J., Nishimura, M., Wang, Y., Sims, J.R., Qiu, S., Savitz, S.I., Salomone, S., and Moskowitz, M.A. (2008). Early release of HMGB-1 from neurons after the onset of brain ischemia. J. Cereb. Blood Flow Metab. *28*, 927–938.

Richard, S., Lapierre, V., Girerd, N., Bonnerot, M., Burkhard, P.R., Lagerstedt, L., Bracard, S., Debouverie, M., Turck, N., and Sanchez, J.-C. (2016). Diagnostic performance of peroxiredoxin 1 to determine time-of-onset of acute cerebral infarction. Sci. Rep. *6*, 38300.

Riddell, J.R., Wang, X.-Y., Minderman, H., and Gollnick, S.O. (2010). Peroxiredoxin 1 stimulates secretion of proinflammatory cytokines by binding to TLR4. J. Immunol. *184*, 1022–1030.

Robinson, M.W., Hutchinson, A.T., Dalton, J.P., and Donnelly, S. (2010). Peroxiredoxin: a central player in immune modulation. Parasite Immunol. *32*, 305–313.

Saksi, J., Ijäs, P., Nuotio, K., Sonninen, R., Soinne, L., Salonen, O., Saimanen, E., Tuimala, J., Lehtonen-Smeds, E.M., Kaste, M., et al. (2011). Gene expression differences between stroke-associated and asymptomatic carotid plaques. J. Mol. Med. (Berl.) *89*, 1015–1026.

Sarrias, M.R., Roselló, S., Sánchez-Barbero, F., Sierra, J.M., Vila, J., Yélamos, J., Vives, J., Casals, C., and Lozano, F. (2005). A role for human Sp alpha as a pattern recognition receptor. J. Biol. Chem. *280*, 35391–35398.

Shawki, H.H., Oishi, H., Usui, T., Kitadate, Y., Basha, W.A., Abdellatif, A.M., Hasegawa, K., Okada, R., Mochida, K., El-Shemy, H.A., et al. (2018). MAFB is dispensable for the fetal testis morphogenesis and the maintenance of spermatogenesis in adult mice. PLoS ONE *13*, e0190800.

Shichita, T., Hasegawa, E., Kimura, A., Morita, R., Sakaguchi, R., Takada, I., Sekiya, T., Ooboshi, H., Kitazono, T., Yanagawa, T., et al. (2012). Peroxiredoxin family proteins are key initiators of post-ischemic inflammation in the brain. Nat. Med. *18*, 911–917.

Shichita, T., Ito, M., Morita, R., Komai, K., Noguchi, Y., Ooboshi, H., Koshida, R., Takahashi, S., Kodama, T., and Yoshimura, A. (2017). MAFB prevents excess inflammation after ischemic stroke by accelerating clearance of damage signals through MSR1. Nat. Med. *23*, 723–732.

Sugisawa, R., Hiramoto, E., Matsuoka, S., Iwai, S., Takai, R., Yamazaki, T., Mori, N., Okada, Y., Takeda, N., Yamamura, K.-I., et al. (2016). Impact of feline AIM on the susceptibility of cats to renal disease. Sci. Rep. *6*, 35251.

Tan, Y.K., Goh, C., Leow, A.S.T., Tambyah, P.A., Ang, A., Yap, E.S., Tu, T.M., Sharma, V.K., Yeo, L.L.L., Chan, B.P.L., and Tan, B.Y.Q. (2020). COVID-19 and ischemic stroke: a systematic review and meta-summary of the literature. J. Thromb. Thrombolysis *50*, 587–595.

Tomita, T., Arai, S., Kitada, K., Mizuno, M., Suzuki, Y., Sakata, F., Nakano, D., Hiramoto, E., Takei, Y., Maruyama, S., et al. (2017). Apoptosis inhibitor of macrophage ameliorates fungus-induced peritoneal injury model in mice. Sci. Rep. *7*, 6450.

Trejo-Gabriel-Galán, J.M. (2020). Stroke as a complication and prognostic factor of COVID-19. Neurologia (Engl. Ed.) *35*, 318–322.

Uchida, K. (2014). Natural antibodies as a sensor of electronegative damage-associated molecular patterns (DAMPs). Free Radic. Biol. Med. *72*, 156–161.

Wang, C., Yosef, N., Gaublomme, J., Wu, C., Lee, Y., Clish, C.B., Kaminski, J., Xiao, S., Meyer Zu Horste, G., Pawlak, M., et al. (2015). CD5L/AIM regulates lipid biosynthesis and restrains Th17 cell pathogenicity. Cell *163*, 1413–1427.

Yamazaki, T., Mori, M., Arai, S., Tateishi, R., Abe, M., Ban, M., Nishijima, A., Maeda, M., Asano, T., Kai, T., et al. (2014). Circulating AIM as an indicator of liver damage and hepatocellular carcinoma in humans. PLoS ONE *9*, e109123.

Yamazaki, T., Sugisawa, R., Hiramoto, E., Takai, R., Matsumoto, A., Senda, Y., Nakashima, K., Nelson, P.S., Lucas, J.M., Morgan, A., et al. (2016). A proteolytic modification of AIM promotes its renal excretion. Sci. Rep. *6*, 38762.

Ziegler, G., Prinz, V., Albrecht, M.W., Harhausen, D., Khojasteh, U., Nacken, W., Endres, M., Dirnagl, U., Nietfeld, W., and Trendelenburg, G. (2009). Mrp-8 and -14 mediate CNS injury in focal cerebral ischemia. Biochim. Biophys. Acta *1792*, 1198–1204.

Zindel, J., and Kubes, P. (2020). DAMPs, PAMPs, and LAMPs in immunity and sterile inflammation. Annu. Rev. Pathol. *15*, 493–518.

Zou, R., Wu, Z., and Cui, S. (2015). Electroacupuncture pretreatment attenuates blood-brain barrier disruption following cerebral ischemia/reperfusion. Mol. Med. Rep. *12*, 2027–2034.

STAR★METHODS

KEY RESOURCES TABLE

REAGENT or RESOURCE	SOURCE	IDENTIFIER
Antibodies		
Rabbit polyclonal anti-AIM (Rab2)	Maehara et al., 2014	N/A
Rat monoclonal anti-mouse AIM (clones 35 and 36)	Yamazaki et al., 2014	N/A
Mouse monoclonal anti-human AIM (clones 6 and 7)	Yamazaki et al., 2014	N/A
Mouse monoclonal anti-HMGB1 (clone GT383)	Gene Tex	Cat#GTX628834; RRID: AB_2888060
Rabbit polyclonal anti-PRDX1	Abcam	Cat#ab41906, RRID: AB_2284360
Goat polyclonal anti-S100A9	R&D Systems	Cat#AF2065; RRID: AB_2184263
Goat polyclonal anti-Iba1	Abcam	Cat#ab5076; RRID: AB_2224402
Mouse monoclonal anti-His tag (Biotin) (clone OGHis)	MBL International	Cat# D291-6; RRID: AB_10897858
Rabbit monoclonal anti-NF-κB p65 (clone D14E12)	Cell Signaling Technology	Cat#8242; RRID: AB_10859369
Rabbit monoclonal anti-Phospho-NF-κB p65 (Ser536) (clone 93H1)	Cell Signaling Technology	Cat#4025; RRID: AB_10827881
Rat monoclonal anti-LAMP2, FITC-conjugated	BD Biosciences	Cat#558758; RRID: AB_397107
Mouse monoclonal anti-MAP2 (clone HM-2)	Sigma-Aldrich	Cat#M9942; RRID: AB_477256
Rat monoclonal anti-CD11b, MicroBeads-conjugated (clone M1/70.15.11.5)	Miltenyi Biotec	Cat#130-049-601
Rat monoclonal anti-CD11b, BV510-conjugated (clone M1/70)	BD Biosciences	Cat#562950; RRID: AB_2737913
Rat monoclonal anti-F4/80, BV421-conjugated (clone T45-2342)	BD Biosciences	Cat#565411; RRID: AB_2734779
Rat monoclonal anti-CD19, BV786-conjugated (clone 1D3)	BD Horizon	Cat#563333; RRID: AB_2738141
Rat monoclonal anti-CD16/32 (clone 93)	Thermo Fisher Scientific	Cat#14-0161-85; RRID: AB_467134
Donkey polyclonal anti-Rabbit IgG (H+L) Highly Cross-Adsorbed Secondary Antibody, Alexa Fluor Plus 405	Thermo Fisher Scientific	Cat#A48258; RRID: AB_2890547
Chicken polyclonal anti-Rabbit IgG (H+L) Cross-Adsorbed Secondary Antibody, Alexa Fluor 488	Thermo Fisher Scientific	Cat#A-21441; RRID: AB_2535859
Chicken polyclonal anti-Mouse IgG (H+L) Cross-Adsorbed Secondary Antibody, Alexa Fluor 647	Thermo Fisher Scientific	Cat#A-21463; RRID: AB_2535869
Goat polyclonal anti-Rabbit IgG (H+L) Cross-Adsorbed Secondary Antibody, Alexa Fluor 405	Thermo Fisher Scientific	Cat#A-31556; RRID: AB_221605
Donkey polyclonal anti-Rat IgG (H+L) Highly Cross-Adsorbed Secondary Antibody, Alexa Fluor 488	Thermo Fisher Scientific	Cat#A-21208; RRID: AB_2535794
Donkey polyclonal anti-Goat IgG (H+L) Cross-Adsorbed Secondary Antibody, Alexa Fluor 647	Thermo Fisher Scientific	Cat#A-21447; RRID: AB_2535864

(*Continued on next page*)

Continued

REAGENT or RESOURCE	SOURCE	IDENTIFIER
Chicken polyclonal anti-Rat IgG (H+L) Cross-Adsorbed Secondary Antibody, Alexa Fluor 594	Thermo Fisher Scientific	Cat#A-21471; RRID: AB_2535874
Goat anti-Human IgG-Fc Fragment Antibody HRP Conjugated	Bethyl	Cat#A80-104P; RRID: AB_67064
Biological samples		
Human infarcted brain tissue	BioIVT	CaseID: 48372; Specimen ID: 1119454B
Chemicals, peptides, and recombinant proteins		
Recombinant mouse PRDX1 (His Tag) protein	Sino Biological	Cat#50552-M08E
Recombinant human PRDX1 (His Tag) protein	Novus Biologicals	Cat#NBC118543
Recombinant mouse PRDX proteins (HA-Tag)	This paper	N/A
Recombinant mouse S100A9 protein	R&D Systems	Cat#2065-S9
Recombinant mouse S100A8/9 protein	R&D Systems	Cat#8916-S8
Recombinant human S100A9 protein	R&D Systems	Cat#9254-S9
Recombinant mouse S100A8 protein	R&D Systems	Cat#9877-S8
Recombinant human S100A8 protein	R&D Systems	Cat#9876-S8
Recombinant human S1008/9 protein	R&D Systems	Cat#8226-S8
Recombinant mouse HSP70 protein	Enzo	Cat#ADI-ESP-502
Recombinant human HSP70 protein	Stress Marq Biosciences	Cat#SPR-117
Recombinant human HMGB1 protein	R&D Systems	Cat#1690-HMB
Recombinant human TLR2-Fc protein	R&D Systems	Cat#1530-TR
Recombinant human RAGE-Fc protein	R&D Systems	Cat#1145-RG
Recombinant mouse and human AIM protein (wild-type and mutants)	Maehara et al., 2014	N/A
Streptavidin, Alexa Fluor 488 conjugate	Thermo Fisher Scientific	Cat#S11223
HRP streptavidin	BD Biosciences	Cat#554066; RRID: AB_2868972
FITC-I	Dojindo	Cat#F-007; CAS: 3326-32-7
4′,6-Diamidine-2′-phenylindole dihydrochloride (DAPI)	Roche	Cat#10236276001; CAS: 28718-90-3
Hoechst33342	Thermo Fisher Scientific	Cat#H3570; CAS: 875756-97-1
TCEP Hydrochloride	Wako	Cat#209-19861; CAS: 51805-45-9
Recombinant mouse AIM/IgM-Fc protein	Hiramoto et al., 2018	N/A
Sudan Black B	Sigma Aldrich	Cat#199664
Oil red-O solution	Muto Pure Chemicals	Cat#40491
G-block	Geno Staff	Cat#GB-01
Critical commercial assays		
HISTOFINE simple stain mouse MAX-PO (R, G, M)	Nichirei Biosciences	Cat#4144341F, 414351F, 414322F
HiLyte Fluor 647 Labeling Kit - NH_2	Dojindo	Cat#LK15
Duolink PLA Fluorescence kit	Sigma Aldrich	Cat#DUO92013, DUO92002
Duolink probe maker MINUS kit	Sigma Aldrich	Cat#DUO92010
TRIzol Reagent	Thermo Fisher Scientific	Cat#15596018
NucleoSpin RNA	MACHEREY-NAGEL	Cat#740955.250
ReliaPrep RNA Miniprep Systems	Promega	Cat#Z6011
SuperScript IV VILO Master Mix	Thermo Fisher Scientific	Cat#4311971

(*Continued on next page*)

Continued

REAGENT or RESOURCE	SOURCE	IDENTIFIER
Experimental models: Cell lines		
Hamster: CHO-S	Thermo Fisher Scientific	Cat#A1155701
Mouse: RAW264.7	ATCC	TIB-71
Human: HEK293T	ATCC	CRL-3216
Experimental models: Organisms/strains		
Mouse: Lysm-Cre;*MafB*$^{-/-}$	Shawki et al., 2018	N/A
Mouse: C57BL6/J	Clea Japan	C57BL/6JJcl
Mouse: *Cd5l*$^{-/-}$ (AIM-deficient)	This paper	N/A
Oligonucleotides		
Primers for QPCR	This paper	Table S1
Recombinant DNA		
pCAGGS-PRDX1, 2, 3, 4, 5, or 6 -HA	This paper	N/A
pCAGGS-mouse or human 2CS mutant	Hiramoto et al., 2018	N/A
pCAGGS-ΔSRCR3	Yamazaki et al., 2016	N/A
pcDNA3.1-mAIM or hAIM	Maehara et al., 2014	N/A
Software and algorithms		
HALO	IndicaLabs	https://indicalab.com/
Evolution Capt	Vilber-Lourmat	https://www.vilber.com/
FACSDiva	BD Biosciences	https://www.bdbiosciences.com/
FlowJo	BD Biosciences	https://www.flowjo.com/

RESOURCE AVAILABILITY

Lead contact

Further information and requests for resources and reagents should be directed to and will be fulfilled by the lead contact, Toru Miyazaki (tm@m.u-tokyo.ac.jp).

Materials availability

All unique reagents generated in this study are available from the lead contact with a completed Materials Transfer Agreement.

Data and code availability

- All data supporting the findings of this study are available within the paper and are available from the lead contract upon request.
- This paper does not report original code.
- Any additional information required to reanalyze the data reported in this paper is available from the lead contact upon request.

EXPERIMENTAL MODEL AND SUBJECT DETAILS

Animals

This study was carried out in strict accordance with the recommendations in the Guide for the Care and Use of Laboratory Animals of the National Institutes of Health. The protocol was approved by the Committee on the Ethics of Animal Experiments of the University of Tokyo (Permit Number: P15-126 and P20-080). All mice were kept under a 12 h light:12 h dark cycle and provided with food and water *ad libitum*. All experimental procedures were performed on 8-14 weeks old male mice. All mouse strains used for analysis were C57BL/6 background. To generate *AIM*$^{-/-}$ mice on a pure C57BL/6 background, two types of the pX335 vectors (Addgene) carrying 5′-caccgaacaatggagccatggccc-3′ or 5′-caccggtgagtgtccctgcttctg-3′ were microinjected into the prenuclei in fertilized eggs of C57BL/6 mice, and thereafter, the 2-cell embryos were transferred into the uterus of pseudo-pregnant female mice. Genomic DNA isolated from the tail of progenies was tested for any deletion within the *Cd5l* (*AIM*) gene locus by PCR and sequencing. An *AIM*$^{-/-}$ mouse line carrying an appropriate deletion at the first ATG region was expanded and used form experiments. Mice were maintained under an SPF condition at the University of Tokyo. Macrophage-specific MafB-deficient mice were obtained by

crossbreeding of Lysm-Cre transgenic mice and *MafB*$^{flox/flox}$ mice as previously described (Shawki et al., 2018) and maintained under a semi-SPF condition at Tsukuba University, Japan.

Primary cell cultures and cell lines

RAW264.7 cells were maintained in Dulbecco's Modified Eagle's Medium (DMEM; Thermo Fisher Scientific) supplemented with 10% of fetal bovine serum (FBS; Thermo fisher Scientific) and 1% penicillin-streptomycin (Thermo Fisher Scientific) at 37°C in a humidified 5% CO2 atmosphere and subjected to the experiments. Primary mouse peritoneal macrophages were prepared from *AIM*$^{-/-}$ mice as follows. After mice were sacrificed, 8 mL of ice-cold PBS with FBS (2.5% v/v) was injected into the peritoneal cavity using 27-g needle. Injected fluid was gently mixed, and then the cell suspension fluid was collected from the peritoneal cavity using 18-g needle attached to a 10 mL syringe. After a centrifugation at 1400 RPM for 5 min, the cells resuspended in DMEM supplemented with 10% FBS and 1% penicillin-streptomycin were plated on a Lab-Tek II chamber slide (NalgeNunk) or 48-well plate (Corning) and cultured for 2 h to let macrophages attach to the slide at 37°C in a humidified 5% CO2 atmosphere. The culture conditions during the experiments are described in the Method Detail section.

METHOD DETAILS

Induction of ischemic stroke (MCAO)

Male mice at 8-14 weeks of age and with 20∼25 g body weight were used for MCAO. According to the procedure of Shichita et al. (2017), a silicone-rubber coated nylon monofilament (Doccol) was inserted into the middle cerebral artery laterally for 45 min under an anesthesia (isoflurane; Pfizer). The cerebral blood flow was monitored using the laser doppler flowmetry (OMEGA) during the MCAO treatment, and mice exhibiting more than 70% reduction in the blood flow at the temporal lobe were used for following experiments (Figure S4). We used only male mice, following the precedents in many reports (Liu et al., 2017; Knowland et al., 2014; Alim et al., 2019).

Antibodies and reagents

Antibodies and reagents used for histological experiments are as follows: Primary antibodies are: AIM (rab2 rabbit polyclonal for IHC of mouse and human brain specimens); #35 and 36 (for mouse AIM ELISA, DAMPs binding assay and recombinant mAIM purification), #6 and 7 (for human AIM ELISA and DAMPs binding assay) established in our laboratory (Yamazaki et al., 2014), partly purchasable from Transgenic Inc.), HMGB1 (clone GT383, Gene-Tex), PRDX1 (rabbit polyclonal antibody, abcam), S100A9 (AF2065, R&D Systems), Iba1 (goat polyclonal antibody, abcam), biotinylated 6xHis tag (D291-6, MBL International), NF-κB p65 (D14E12, Cell signaling technology), phospho-NF-κB p65 (93H1, Cell signaling technology), LAPM-2 (clone ABL-93, BD Biosciences) and CD11b microbeads (clone: M1/70.15.11.5, Miltenyi Biotec). Secondary antibodies and related reagents are: Alexa fluor 405, 488,594 or 647 conjugated anti-rabbit, rat, goat or mouse IgG (Thermo Fisher Scientific), anti-human IgG-Fc-HRP (A80-104P, Bethyl laboratories, Inc.), Streptavidin-Alexa fluor 488 (Thermo Fisher Scientific), Streptavidin-HRP (554066, BD Biosciences), DAPI (Roche) or Hoechst33342 (Thermo Fisher Scientific), G-Block (Genostaff, Tokyo, Japan) and HISTOFINE simple stain mouse MAX-PO (R) (NICHIREI Biosciences). Specimens were analyzed using a microscope: IXPlore and a research slide scanner: SLIDEVIEW VS200 (Olympus) or a confocal microscope: FV10i-DOC. Antibodies used for flowcytometry are as follows: BV510 rat anti-CD11b (M1/70, BD Biosciences), BV421 rat anti-mouse F4/80 (T45-2342, BD Biosciences), BV786 rat anti-CD19 (1D3, BD Biosciences), and purified rat anti-mouse CD16/CD32 (2.4G2, Fc Block, Thermo Fisher Sciences). Fluoresceinisothiocyanate isomer-I (FITC-I) and HiLyte Fluor 647 Labeling Kit-NH2 (Dojindo) were used for protein labeling.

DAMPs and related proteins

Mouse PRDXs with a HA tag that were used in the binding assays were generated in house. They were produced in HEK293T cells by transfecting pCAGGS subcloned with cDNA for mouse PRDX1, 2, 3, 4, 5 or 6 tagged with HA peptides and thereafter purified from cell lysates using an anti-HA antibody column. Other DAMPs and related proteins were purchased as follows. Mouse PRDX1-His (50552-M08E, Sino Biological), human, PRDX1-His (NBC118543, Novus Biologics), mouse S100A8 (9877-S8-050, R&D Systems), mouse S100A9 (2065-S9-050, R&D Systems), mouse S100A8/A9 (8916-S8-050, R&D Systems), human S100A8 (9876-S8-050, R&D Systems), human S100A9 (9254-S9-050, R&D Systems), human S100A8/A9 (8226-S8-050, R&D Systems), mouse HSP70-A1 (low endotoxin; ADI-ESP-502-D, Enzo), human HSP70 (Endotoxin Free; SPR-117A, StressMarq), human HMGB1 (1690-HMB-050, R&D Systems), mouse TLR2-Fc (1530-TR, R&D Systems), human RAGE-Fc (1145-RG, R&D Systems) .

CD11b^{+} cell isolation from brain

Dissociation of brain tissue

Mice were perfused with PBS transcardially under deep anesthesia by using Isoflurane (Pfizer). Brain tissues were excised, and the infarcted or non-infarcted side of the brains were cut into small pieces, then the pieces were treated with the enzyme solution containing 2.5 U/mL Collagenase D, 8.5 U/mL Dispase, 25 mg/mL DNase I and Complete Mini (Roche) in 1xHBSS at 37°C for 1 h. The digested tissue was passed through a18 G-needle several times and filtrated through a 70-μm strainer (Miltenyi Biotec), thereafter centrifuged at 400 g for 15 min at 4°C. The cell-pellets were resuspended in 35% Percoll in PBS and centrifuged at 800 g for 45 min at

4°C. The pellets were resuspended in 0.5% FBS in PBS. Finally, $CD11b^+$ cells within the total cells were isolated using the CD11b Microbeads (Miltenyi Biotec), according to the manufacturer's protocol.

EILSA for AIM

All ELISA assays were performed in duplicated manner. Mouse AIM in the brain tissue lysate was measured by ELISA using two different rat anti-mouse AIM monoclonal antibodies (rat IgG, clone #35 and 36; generated in our laboratory). The inter-assay coefficients of variation assessed by using a C57BL/6 mouse serum was 4.8% for mouse AIM, and the intra-assay coefficients of variation was always less than 4.1%. The lower limit of quantification assessed by using recombinant AIM protein as a standard was 0.0625 ng/ml for mouse AIM.

Production and purification of rAIM and related proteins

CHO-Scells were transfected with pcDNA3.1-mAIM or hAIM plasmid and cultured in CD Forti CHO medium (Thermo Fisher Scientific) for 3 days. rAIM was purified from culture supernatant using rat anti-mouse AIM monoclonal antibody #36 (for mouse AIM) or mouse anti-human AIM monoclonal antibody #7 (for human AIM) conjugated HiTrap NHS-activated HP Columns (Cytiva). Bound protein was eluted with 0.1 M Glycine-HCl, pH 2.5 and neutralized with 1 M Tris-HCl, pH 8.5. Protein was concentrated as necessary using Amicon Ultra filter concentrators (Millipore), and stored at −80°C in PBS. Endotoxin levels were measured by Limulus Color KY Test Wako (Fujifilm Wako Chemicals) following the manufacturer's protocols. Protein concentration was determined by the BCA (bicinchoninic acid) assay according to the manufacturer's protocol (Pierce). The 2CS mutant was created by substituting the cysteine at 194 (in mouse AIM) and 191 (in humans AIM) to serine (TGC to TCC in nucleotides) (Hiramoto et al., 2018). The ΔSRCR3 mutant was generated by deleting amino acids of the SRCR3 domain (starting from the aspartic acid at 242 to the valine at 352) in mouse AIM (Yamazaki et al., 2016; Hiramoto et al., 2018). Each mutant cDNA was subcloned into the pCAGGS expression vector. Production and purification of mutant AIM was performed as for the wild-type rAIM. Recombinant AIM/IgM-Fc and IgM-Fc proteins were generated as described previously (Hiramoto et al., 2018).

Evaluation of binding efficiency of AIM to DAMPs

96-well ELISA plates were coated with DAMPs and control proteins resolved in Bicarbonate buffer (0.1 M $NaHCO_3$/ Na_2CO_3, pH 9.6) at 2 μg/mL unless otherwise specified O/N at 4°C. After the plates were washed with tris buffered saline-tween (TBS-T) four times, they were coated with blocking buffer (1% Casein/TBS) for 2 h at RT. After a wash with TBS-T, AIM resolved in a dilution buffer (0.2% Casein/ TBS/2 mM $CaCl_2$) at various concentrations was added to the well and plates were incubated for 1 h at RT. After 5-times wash with TBS-T/2 mM $CaCl_2$, biotinylated anti-mouse or human AIM antibody (clone #35 for mouse, clone 7 for human) was added to the wells and incubated for 1 h at RT. After 4-times wash with TBS-T/2 mM $CaCl_2$, the Streptavidin-HRP diluted in 0.2% Casein/ TBS/2 mM $CaCl_2$ was added to the wells and incubated for 1 h at RT. After 4-times wash with TBS-T/2 mM $CaCl_2$, TMB was added and incubated at RT for 10-25 min. The reaction was stopped by adding 1 N H_2SO_4 and thereby the absorbance at OD 450 nm was analyzed using a multiple plate reader.

To assess the binding mode by immunoblotting, mouse rAIM was incubated with either mouse S100A9, mouse PRDX1, or human HMGB1 resolved in TBS/2 mM $CaCl_2$ at 4°C O/N. Proteins were loaded on SDS-PAGE in non-reducing condition and transferred to a PVDF-membrane. The membrane was then treated with a blocking buffer (5% skim milk inTBS-T) for 1 h at RT, thereafter, with the anti-mouse AIM polyclonal antibody (rab2) at 4°C O/N. After 3-times washes with TBS/2 mM $CaCl_2$, the goat anti-rabbit IgG conjugated with HRP that was diluted in the blocking buffer was loaded on the membrane for 1 h at RT. After 3-times washes, the membrane was treated with the Immobilon Forte Western HRP Substrate (EMD Millipore Corporation), and thereafter, the enhanced luminescence signals were examined using FUSION FX (Vilber-Lourmat). The molecular weight of each signal was calculated by the Evolution Capt software (Vilber Lourmat).

Proximity ligation assay (PLA)

PLA was performed using Duolink PLA Fluorescence kits according to the protocol of the manufacturer (Sigma Aldrich). The anti-PRDX1 antibody was conjugated with the MINUS probe using the Duolink probe maker MINUS kits (Sigma Aldrich). Briefly, the brain tissue was fixed in 4% paraformaldehyde (PFA) for 24 h and embedded in paraffin. For PLA of AIM/PRDX1, brain sections were treated with Proteinase K to retrieve antigen, thereafter, incubated with the rabbit anti-AIM polyclonal antibody (rab2) overnight at 4°C. Next day, sections were incubated with anti-rabbit PLUS probe for 1h at 37°C, washed, and then treated with the anti-PRDX1 antibody conjugated with the MINUS probe. After incubation for 1h at 37°C, sections were treated with the ligation reagent for 30 min and then with the amplification reagent for 100 min at 37°C. Samples were mounted with the Duolink *In Situ* Mounting Media with DAPI.

In vitro evaluation of DAMPs captures by macrophage

Peritoneal macrophages isolated from $AIM^{-/-}$mice were plated on a Lab-Tek II chamber slide (NalgeNunk) and cultured for 2 h to let them attach to the slide. The cells were incubated with 10 μg/mL of DAMPs (mouse PRDX1-His, human PRDX1-His, human HMGB1, or mouse S100A9) with or without wild-type mouse or human rAIM (100 μg/mL) in DMEM supplemented with 5% FBS at 37°C for 10 min. For mouse PRDX1, the mutants of 2CS, ΔSRCR3 were also used. After an incubation, the cells were washed with PBS

for 3 times and fixed with 4% PFA/PBS for 15 min. Each ligand and AIM were immunostained with antibodies to His (for mouse and human PRDX1), HMGB1 or S100A9, and AIM, followed by fluorescent-conjugated secondary antibodies. Nuclei were stained with 4',6-diamidino-2-phenylindole (DAPI). The cells were analyzed under a florescence confocal microscope.

Flowcytometry

Peritoneal cells isolated from *AIM*$^{-/-}$ mice were cultured on a 48-well plate in the presence of HyLyte Fluor 647-labled mouse or human AIM (10 μg/mL) and FITC-labeled mouse PRDX1, mouse S100A9 or human HMGB1 (2.5 μg/mL) in DMEM supplemented with 5% FBS for 15 min at 37°C. Thereafter, cells were harvested in 4 mL round bottomed tubes. After Fc receptors were blocked with anti-mouse CD16/32, the cells were stained for F4/80, CD11b and CD19 for the surface expression. Fluorescent intensity for FITC (DAMPs) and HyLyte Fluor 647 (AIM) within the cells positive for CD11b and F4/80 and negative for CD19 were analyzed by flowcytometory (BD FACSCelesta, BD Biosciences). BD FACSDiva and FlowJo (BD Biosciences) were used for analysis.

NFκB activation assay

RAW264.7 cells were incubated with mouse S100A9 or RPDX (5 μg/mL) resolved in DMEM+0.1% FBS in the presence or absence of mouse rAIM (10 μg/mL) in 96-well cell culture plates for 30 min at 37°C. After a wash with PBS, cells were lysed using by loading buffer containing SDS, boiled and loaded on an SDS-PAGE gel. Thereafter, the phosphorylation of NFκB was analyzed by immunoblotting using and anti-phospho- NFκB p65 antibody (3033S, Cell Signaling Technology). Total NFκB was also analyzed using an anti- NFκB p65 antibody (8242S, Cell Signaling Technology).

Histology

AIM detection and other IHC at infarcted brain

Brain tissue was excised and fixed in 4% PFA in PBS for 24 h, thereafter embedded in paraffin. 6 μm sections were immunostained with the rabbit anti-AIM polyclonal antibody (rab2; available for human and mouse AIM), followed by incubation with HITOFINE simple stain mouse MAX-PO (R) (NICHIREI Biosciences) for 30 min. After stained with diaminobenzidine tetrahydrochloride (DAB), sections were counter-stained with hematoxylin. To block autofluorescence, slides were incubated with 0.5% Sudan Black B (199664, Sigma Aldrich) diluted with 70% ethanol for 25 min before immunostained. *DAMPs staining*: Sections were immunostained with a rabbit anti-PRDX1 polyclonal antibody (ab41906), mouse anti-HMGB1 monoclonal antibody (GTX628834), or goat anti-S100A9 polyclonal antibody (AF2065), followed by incubation with HISTOFINE simple stain mouse MAX-PO (R, M, or G) for 30 min. *MAP2 and Iba1 detection*: Sections were immunostained with a mouse anti-MAP2 monoclonal antibody (M9942) or goat anti-Iba1 polyclonal antibody (ab5076), followed by incubation with HISTOFINE simple stain mouse MAX-PO (M or G) for 30 min. Before the reaction with primary antibodies, sections were treated in each condition for antigen retrieval. S100A9, HMGB1, and MAP2: Boiled Tris/ EDTA buffer (pH 9.0) containing 0.05% Tween-20 for 20 min. PRDX1: 20 μg Protenase K in PBS at 37°C for 20 min. Iba1: Boiled citrate buffer (10 mM, pH 6.0) containing 0.05% Tween-20 for 20 min. After stained with DAB, sections were counter-stained with hematoxylin. *Oil red-O staining*: Brain tissues were fixed in 4% paraformaldehyde (PFA) in PBS for 24 h and 30% sucrose solution for 24∼48 h and were frozen with OCT compound. 10 μm sections were stained with Oil red-O solution (Muto Pure Chemicals). The histologic data for human brain AIM were purchased from Genostaff Co. Ltd, who had obtained a commercially available paraffin block of a brain tissue from human stroke patient from BioIVT and stained the serial sections for human AIM and MAP2.

Quantification of DAMPs in brain

DAMPs-DAB staining images were obtained and digitally captured using slide scanner VS200 (OLYMPUS) with a 20x objective lens. Digital image analysis was performed with commercial software HALO (IndicaLabs). DAB and hematoxylin signals were detected using object colocalization-based algorithms, and the amount of extracellular DAMPs were estimated by subtracting the hematoxylin-colocalizing DAB signals from the total DAMPs signals.

Evaluation of neurologic deficits (neurologic score)

Behavioral assessments were performed every 24 h after MCAO. The neurologic deficits were scored as previously described (Jiang et al., 2005). The criteria is summarized as follows: 0 point: normal; 1 point: mild turning behavior with/without inconsistent curling when picked up by tail, < 50% attempts to curl to the contralateral side; 2 points: mild consistent curling, > 50% attempts to curl to contralateral side; 3 points: strong and immediate consistent curling, mouse holds curled position for more than 1-2 s, the nose of the mouse almost reaches tail; 4 points: severe curling progressing into barrelling, loss of walking or righting reflex; 5 points: comatose or moribund.

Quantitative PCR assay

Total RNA from brain tissue was extracted using TRIzol Reagent (Thermo Fisher Scientific) and purified with NucleoSpin RNA (MACHEREY-NAGEL). Total RNA from CD11b^{+} cells was extracted using ReliaPrep RNA Miniprep Systems (Promega). Using the RNA, cDNA was prepared using SuperScript IV VILO Master Mix (Thermo Fisher Scientific). The quantitative evaluation of mRNA was performed by the $\Delta\Delta C_T$ method using Power SYBR Green PCR Master Mix (Thermo Fisher Scientific) with a QuantStudio 3 Real-Time PCR system (Thermo Fisher Scientific). Sequences of the oligonucleotides used are listed in Table S1.

QUANTIFICATION AND STATISTICAL ANALYSIS

Data were analyzed using BellCurve for Excel (Social Survey Research Information) and presented as mean values ± s. d. unless otherwise specified. All data were analyzed by two-sided test. Paired results were assessed using Welch's t test. Comparisons between multiple groups were analyzed using one-way or multi-way ANOVA followed by the Bonferroni's post hoc test. For the Kaplan-Meier curves, *P value*s were determined with the Generalized Wilcoxon test. Unless otherwise specified, the significance code is as added in each Figure legend. Number of samples (n) is found in each Figure legend.